UNIVERSITY
OF TURKU

# $Al^{18}F$-NOTA-folate PET for imaging of inflammation in calcific aortic valve disease

Institute of Biomedicine
MDP in Biomedical Sciences, Drug Discovery and Development
Master's thesis

Author:
Erki Malmer

Supervisors:
PhD Mia Ståhle
Professor Anne Roivainen

14.04.2025
Turku

# Abstract:

**Subject**: Institute of Biomedicine, MDP in Biomedical Sciences, Drug Discovery and Development
**Author(s)**: Erki Malmer
**Title**: Al$^{18}$F-NOTA-folate PET for imaging of inflammation in calcific aortic valve disease
**Supervisor(s)**: PhD Mia Ståhle, Professor Anne Roivainen
**Number of pages**: 57 pages
**Date**: 9.4.2025

Calcific aortic valve disease (CAVD), along with its clinical presentation as aortic valve stenosis (AS), especially affects elderly population. The progression of AS occurs in two stages: an initial phase characterized by endothelial injury, lipid accumulation, and inflammation, followed by a subsequent phase dominated by calcification-promoting factors. Macrophages are central to both the inflammatory response and the advancement of calcification.

Folate receptor beta (FR-β), expressed on activated macrophages, has been targeted for positron emission tomography (PET) imaging to detect inflammation in atherosclerosis and autoimmune myocarditis. However, its use in CAVD has not been explored. The aim of this study was to evaluate whether a PET tracer Al$^{18}$F-NOTA-folate enables detection of inflammation in experimental CAVD.

LDLR-/-ApoB100/100 mice on a high-fat diet for 8 months (CAVD model) and age-matched controls were studied. Echocardiography was performed to assess the AS severity. Then mice underwent both $^{18}$F-NaF (microcalcification) and Al$^{18}$F-NOTA-folate PET imaging. Al$^{18}$F-NOTA-folate uptake was further analysed with ex-vivo autoradiography and immunohistochemistry.

Echocardiography demonstrated significant AS in the CAVD compared to controls. Moreover, PET imaging with Al$^{18}$F-NOTA-folate revealed higher uptake in CAVD valve leaflets compared to controls and immunohistochemistry identified continuous Mac-3 positive macrophage areas in CAVD valves.

In conclusion Al$^{18}$F-NOTA-folate PET can detect inflammation in the aortic valve region of an experimental CAVD mouse model and may be a promising tool for assessing early-phase disease. However, further detailed investigation is needed to determine the precise origin of the signal observed in PET/CT imaging.

**Keywords**: Calcific aortic valve disease (CAVD), Al$^{18}$F-NOTA-folate PET, folate receptor beta (FR-β), macrophages.

# Table of contents

**Abstract:** 2

**1 Introduction** 5

**1.1 Calcific aortic valve disease (CAVD)** 6

1.1.1 Morphology and function of the aortic valve 6

1.1.2 Clinical manifestation of CAVD 7

1.1.3 Pathophysiology of CAVD 8

1.1.4 Current therapies and its challenges in CAVD 11

**1.2 Management of patients with aortic stenosis** 13

1.2.1 Echocardiography and diagnosis of aortic stenosis 13

1.2.2 Molecular imaging 15

**1.3 Macrophages and folate receptor-β (FR-β)** 17

1.3.1 Nature of macrophages 17

1.3.2 Macrophage FR-β as an imaging target 19

**1.4 Aims and hypotheses** 21

**2 Results** 22

**2.1 Echocardiography** 22

**2.2 In vivo PET/CT imaging and biodistribution** 24

**2.3 Autoradiography** 28

**2.4 Immunohistochemical staining** 30

**2.5 Correlations of echocardiography and Al$^{18}$F-NOTA-folate uptake with histological findings** 32

**3 Discussion** 34

**3.1 Development of aortic stenosis in CAVD mice** 34

**3.2 Al$^{18}$F-NOTA-folate uptake in the aortic valve** 35

**3.3 Macrophages and microcalcification related to early phase of CAVD** 37

**3.4 Evaluating association between the echocardiography and Al$^{18}$F-NOTA-folate uptake with histological findings** 39

**3.5 Considerations on mouse models** 40

**3.6 Translational aspects** 41

**3.7 Conclusions** 42

4 Materials and methods 43

4.1 Design of the study 43

4.2 Echocardiography 44

4.3 Radiochemistry 44

4.4 *In vivo* PET/CT imaging and biodistribution 45

4.5 *Ex vivo* autoradiography, histology, and immunostaining 46

4.6 Statistical methods 47

5 Acknowledgements 48

6 Abbreviations 49

References 51

# 1 Introduction

Calcific aortic valve disease (CAVD), and its clinical manifestation aortic valve stenosis (AS), is the most prevalent heart valve disease, especially in elderly people. Due to the causal relationship between aging and the incidence of AS, the prevalence of AS is expected to double in the coming decades as life expectancy increases and the population ages. (Coffey et al., 2014; d'Arcy et al., 2016; Osnabrugge et al., 2013)

In addition to aging, the main risk factors for CAVD are male sex, obesity, hypertension, smoking, diabetes mellitus, and elevated plasma lipoprotein(a) [Lp(a)] and low-density lipoprotein (LDL). Genetic factors also have crucial role in the development of CAVD as it is observed that individuals with a sibling who has a history of AS have significantly higher risk of developing the disease. (Moncla et al., 2023) Moreover, aortic valve malformations, such as unicuspid or bicuspid valves, are major risk factors and the incidence of disease in these conditions is almost universal and generally more rapid. (Pawade et al., 2015)

In most cases, CAVD is asymptomatic and often remains underdiagnosed until the disease has progressed to a severe, symptomatic stage. (Jain et al., 2024) Additionally, left ventricular hypertrophy (LVH) is commonly associated with AS increasing the risk of heart failure. Pathophysiology of AS comprises highly complex processes and it is commonly separated into two phases. An early initiation phase with endothelial damage, lipid deposition, and inflammation, resembling atherosclerosis, followed by a later propagation phase predominated by pro-fibrotic and pro-calcific factors. (Pawade et al., 2015; Rajamannan et al., 2011).

Although AS is the most common type of valvular disease and presents an increasing healthcare burden, there are currently no medical therapies available to cure or slow its progression. (Pawade et al., 2015) At the moment only known effective treatment for symptomatic and severe AS is aortic valve replacement (AVR) operation (Otto et al., 2021). Evaluation of AS relies mainly on structural and functional alterations in the aortic valve, while overlooking physiological changes, such as inflammation, which is closely linked to the development of aortic stenosis.

## 1.1 Calcific aortic valve disease (CAVD)

### 1.1.1 Morphology and function of the aortic valve

The aortic valve is a semilunar valve consisting of three cusps, located between the left ventricular (LV) and the ascending aorta. These cusps are anchored to the aortic root through the aortic annulus, which provides support for the valve. The valve's cusps are held in place by fibrous structures known as commissures. Additionally, the names of the cusps are associated with the coronary arteries that originate from the sinuses. (Crawford et al., 2023)

The main role of the aortic valve is to prevent the backflow of oxygenated blood into the LV. During systole, when the heart contracts, the pressure inside the LV is higher compared to the aortic pressure, leading to aortic leaflets to open and enabling sufficient blood flow from LV into the ascending aorta. During diastole, when the heart relaxes, the pressure in the LV decreases below the aortic pressure, causing the leaflets to close and prevent backflow of blood into the LV. (Crawford et al., 2023)

The aortic valve is tri-layered structure consisting of the fibrosa, spongiosa and ventricularis, surrounded by an endothelial layer. Fibrosa is collagen-rich layer located on the aortic side and responsible of the mechanical behaviour of the leaflets. As the name implies, the ventricularis is located on the ventricular side and is the thinnest layer having elastin content that allows sufficient movement of the valve. Spongiosa is located between these two layers comprising aggregates of proteoglycans and glycosaminoglycans, that serves hydration, mechanical absorption and structural support to the leaflets. (Grego-Bessa et al., 2010)

The aortic valve endothelium consists of valvular endothelial cells (VECs) that line the aortic valve leaflets. VECs have important role in maintaining valvular homeostasis by forming tight junctions that limit the influx of pathogens into the valve. VECs are exposed to different forces of blood flow, which translate into biological stress responses such as cellular signalling, extracellular matrix (ECM) remodelling, and inflammatory responses. These stress signals are released from VECs and can future stimulate valvular interstitial cells (VICs). (Bartoli-Leonard et al., 2021)

VICs are the most common cell type in the aortic valve, present in all three layers. These fibroblast-like cells originate from both valve VECs and the cardiac neural crest. VICs main role is to maintain the structural integrity of the valve. There is significant crosstalk between

VICs and VECs. For instance, VECs are responsible for maintaining the resting state of VICs by releasing inhibitory cytokines during normal blood flow (Butcher & Nerem, 2006) and VICs inhibits VECs` endothelial-to-mesenchymal transition (EndMT). The EndMT is a process initiated by various stimuli, such as inflammation or injury, where endothelial cells transform into mesenchymal cells with a more migratory and fibroblastic phenotype, which can play a role in tissue remodelling and fibrosis. (Hjortnaes et al., 2015)

### 1.1.2 Clinical manifestation of CAVD

In most cases, CAVD is asymptomatic and often remains underdiagnosed until the disease has progressed to a severe, symptomatic stage, in which the aortic valve leaflets are thickened due to deposition of collagen and calcification. This leads to gradual valve narrowing and an increase in transvalvular blood flow velocity, a condition known as AS. The most common symptoms of severe aortic stenosis are often shortness of breath, chest pain, fatigue, syncope, and palpitations, with oedema usually appearing in more advanced stages when heart failure has developed. Moreover, in symptomatic cases, AS is characterized by progressively worsening cardiorespiratory symptoms with rapid decline. (Jain et al., 2024)

The area of a healthy aortic valve ranges from 3 to 4 $cm^2$. Initial symptoms of disease typically appear when the valve area narrows to less than 1 $cm^2$. One reason to asymptomatic nature of CAVD is the heart's compensatory mechanisms. As the aortic valve area decreases, the LV pressure increases to compensate for the narrowed aorta. This leads to elevated blood flow velocity through the aortic valve and higher systolic pressure in the LV compared to the aorta, which are two main characteristics of AS disease. (Bornstein et al., 2023)

Increased systolic pressure in the LV initiates myocardial cells to enhance protein synthesis. This leads to concentric LVH, where the LV wall becomes thicker without enlargement of the LV cavity. Due to increased wall thickness and reduced wall stress, LVH was historically considered advantageous for cardiac performance in AS disease. However, the elevated workload of the heart, altered diastolic filling, and LVH increase myocardial fibrosis. These factors will lead to increased ischemia of the heart by raising the oxygen demand and reducing the oxygen supply. For these reasons, the concept of beneficial LVH is being challenged. (Bornstein et al., 2023; Rader et al., 2015; Stein et al., 2022) Moreover, it has been demonstrated that earlier intervention in AS patients without LVH could be more beneficial compared to those with LVH because of increased risk of heart failure at the end stage of the disease (Gonzales et al., 2020).

Lp(a) is gaining recognition as an independent risk factor in the development of CAVD. Studies have associated Lp(a) levels to both microcalcification and macrocalcification of the aortic valve. Moreover, elevated Lp(a) concentrations may accelerate the progression of aortic stenosis. Its impact on CAVD is especially notable in younger, otherwise healthy individuals. (Kronenberg et al., 2022)

Lp(a) levels are primarily influenced by genetic factors (Kronenberg et al., 2022). High concentrations of Lp(a), along with the proteins it carries, have been shown to induce inflammatory and calcification-related genes in VICs, contributing to an increased incidence and progression of AS. Lp(a) is a major carrier of oxidized phospholipids (OxPLs), which play a key role in the pro-inflammatory and pro-calcific effects. Furthermore, OxPLs have been shown to promote the transendothelial migration of monocytes and trigger gene expression associated with osteoblastic processes in VICs. (Zheng et al., 2019)

### 1.1.3 Pathophysiology of CAVD

The pathophysiology of CAVD consists of two phases. The early initiation phase is identified by endothelial damage, lipid accumulation, and inflammation, sharing similarities with atherosclerosis. It is followed by a later propagation phase, dominated by pro-fibrotic and pro-calcific factors that accelerate disease progression, eventually leading to valve narrowing and obstruction to LV outflow. (Pawade et al., 2015; Rajamannan et al., 2011)

CAVD is believed to be initiated by increased mechanical stress and reduced shear stress. Importantly, calcification mainly develops on the fibrosa side of the valve, where disturbed flow is observed. This disturbed flow, along with elevated levels of blood lipids and monocytes, contributes to endothelial injury. Additionally, disrupted blood flow and high lipid levels induce VECs to undergo the EndMT process (Figure 1). During EndMT, VECs become activated, which enhances lipid and immune cell infiltration, ultimately leading to VEC dysfunction. The increased infiltration of immune cells and lipids, particularly Lp(a) and LDL cholesterol, initiates an inflammatory reaction in the valve (Figure 1). This inflammatory reaction is primarily mediated by macrophages but also involving T lymphocytes and mast cells. Although inflammation driven by proinflammatory cytokines is beneficial in tissue injury and pathological conditions, it becomes overactive in CAVD, leading to chronic, pathological inflammation. (Bartoli-Leonard et al., 2021)

Despite multiple cell types in the aortic valve is able to differentiate into osteoblast-like cells, the most likely source of these cells are VICs (Liu et al., 2007). It has been observed that in the early stage of CAVD, the differentiation of VICs into osteoblast-like cells is coordinated by macrophages through several proinflammatory cytokines, such as interleukin (IL) 1β, IL-6, IL-8, tumour necrosis factor, and insulin-like growth factor-1. (Aikawa et al., 2007). In the later stage of this differentiation is again dominated by several pathways related to calcific processes for instance, Notch, Wnt/ β-catenin, and receptor activator of nuclear factor kappa B. (Pawade et al., 2015)

There are different subtypes of VICs, and the most important ones related to CAVD are: quiescent VICs (qVICs), activated myofibroblast-like VICs (aVICs), endothelial-derived VICs (eVICs), and osteoblastic VICs (oVICs) (Liu et al., 2007). In a healthy aortic valve, where the structure and function of the leaflets are normal, the most prominent cell type is qVICs. Changes in blood flow can alter this situation by promoting the differentiation of qVICs into aVICs. aVICs are responsible for the remodelling of the valve's ECM. Under normal conditions, aVICs differentiate back into qVICs, which is a hallmark of valve homeostasis. However, under pathological conditions, these aVICs can differentiate into oVICs, which are involved in calcium deposition in CAVD. It has also been demonstrated that VECs can differentiate into eVICs via the EndMT process if the interaction between VICs and VECs is disturbed. These EndMT-derived eVICs accumulate within the valve leaflets and can differentiate into oVICs, further contributing the pathological ECM remodelling seen in CAVD. (Figure 1). (Hjortnaes et al., 2015)

Microcalcification is also associated with the early stages of CAVD progression and has been observed to colocalize with sites of lipid deposition. It is believed that microcalcification is driven by cell death and the release of apoptotic bodies in these regions. These apoptotic bodies resemble matrix vesicles found in bone and contain components for hydroxyapatite crystal formation. Furthermore, these hydroxyapatite formations enhance the proinflammatory response from macrophages, creating a positive feedback loop of inflammation and calcification. (Nadra et al., 2005; Pawade et al., 2015)

Another feature of CAVD is neovascularization, the process leading to formation of new blood vessel. Healthy aortic valves are avascular whereas in CAVD, micro-vessels and arterioles develop to sustain diseased tissue as fibrosis and calcification impair nutrient supply. Histological analyses have revealed subpopulation of cells expressing endothelial markers, endothelial growth factor receptor and smooth muscle α-actin in calcified valves. Moreover, it has been observed that inflammatory cells, especially mast cells, release factors that stimulate vascular endothelial growth factor production in myofibroblasts, enhancing proangiogenic factor levels at the site. (Chalajour et al., 2007; Syväranta et al., 2010)

In the propagation phase of CAVD pathophysiology, similar structural processes are seen as in skeletal bone formation (Pawade et al., 2015). Firstly, the collagen is accumulated in the valve for the pro-calcific processes via aVICs ECM remodelling. This collagen accumulation is thought to be initiated due to reduced nitric oxide expression because of the endothelial damage (El Accaoui et al., 2014).

Angiotensin-converting enzyme is upregulated in CAVD, highlighting the renin-angiotensin system’s role in collagen formation. In the valve, Angiotensin-converting enzyme mediates profibrotic effects by converting angiotensin I to angiotensin II via the angiotensin II type 1 receptor. While angiotensin II can also exert antifibrotic effects through the type 2 receptor, CAVD predominantly favours angiotensin II type 1 receptor, promoting fibrosis. Furthermore, while angiotensin-converting enzyme type 2 demonstrates antifibrotic and anti-inflammatory effects through the Ang1-7/Mas pathway, this pathway is found to be downregulated in CAVD. (Peltonen et al., 2011)

After this pro-fibrotic process, CAVD progression continues with valvular calcification utilizing properties of VICs which eventually develop osteogenic phenotype. Studies have shown that increased expression levels of several osteoblast-specific proteins, such as Cbaf1/Runx2 transcription factor, are observed in CAVD. (Rajamannan et al., 2003). Additionally, several ECM proteins associated with skeletal bone formation, for example osteopontin and bone-sialoprotein, are observed in CAVD (Pawade et al., 2015)

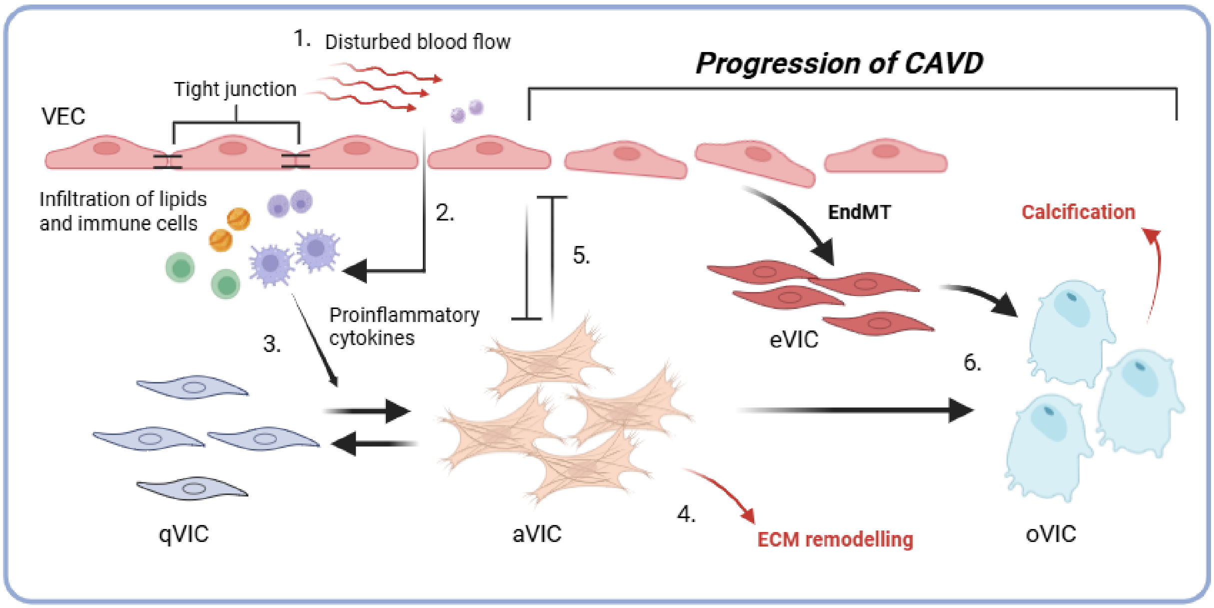

**Figure 1. Inflammation associated with the early phase of CAVD and disease progression.** Simplified illustration of inflammation related processes in CAVD development and progression: 1. CAVD is thought to be initiated by disturbed blood flow due to elevated lipid plasma concentrations and blood pressure, which alter the integrity of valvular endothelial cell (VEC) connections. 2. The "leaky" VEC layer enables the infiltration of lipids and immune cells. 3. Oxidized lipids within immune cells, through pro-inflammatory cytokines, contribute the differentiation of quiescent valvular interstitial cells (qVICs) to activated valvular interstitial cells (aVICs), which resemble myofibroblast cells. 4. These aVICs modify the extracellular matrix (ECM) by increasing the collagen content in the leaflets. In healthy leaflets, these aVICs differentiate back to qVICs, whereas in CAVD, aVICs continue ECM remodelling and contribute to the development of CAVD by affecting the flexibility of the leaflets. 5. There is significant crosstalk between VICs and VECs via inhibitory cytokines during normal blood flow. In contrast, this crosstalk is reduced as qVICs differentiate to aVICs, causing VECs to undergo endothelial-to-mesenchymal transition (EndMT). 6. This EndMT process within aVICs differentiates to osteoblast-like valvular interstitial cells (oVICs), promoting disease progression and leading to fibrotic and calcified leaflets, causing obstruction of blood flow in the aorta. *Edited from (Hjortnaes et al., 2015) and created using BioRender.*

### 1.1.4 Current therapies and its challenges in CAVD

Although AS is the most prevalent type of valve disease and presents an increasing healthcare burden, there are currently no medical therapies available to cure or slow its progression. (Pawade et al., 2015). At the moment only known effective treatment for severe AS is AVR, performed either through open-heart surgery or a transcatheter procedure. (Otto et al., 2021). It is estimated that 150,000 AVR operations are performed annually in the United States, while globally, approximately 350,000 AVRs are performed each year, resulting in a total loss of 1.8 million disability-adjusted life years annually (Roth et al., 2020).

Transcatheter AVRs have demonstrated to be safe procedures with low procedural complications and low morbidity. However, even after a successful AVR, the risk of heart failure remains high. AVRs are typically performed only in patients with severe and symptomatic disease. Consequently, there has been increasing interest in whether earlier AVR in asymptomatic AS might improve patient outcomes. (Lindman & Lindenfeld, 2021; Vemulapalli Sreekanth et al., 2019) While this strategy may improve patient outcomes, its effectiveness is limited by the oversimplification of AS as purely a mechanical disease that can only be addressed with a mechanical solution (Lindman et al., 2021).

While the role of mechanical stress remains central, growing evidence shows that AS is characterized by highly regulated and tightly controlled biological processes (Pawade et al., 2015). These complex mechanisms not only deepen the understanding of AS but also highlight potential targets for therapeutic intervention.

Due to the involvement of lipid deposition, inflammation, and calcification, and the similar pathophysiological features shared between CAVD and atherosclerosis, it was hypothesized that statins would be beneficial for patients with AS. However, clinical trials did not observe any halt or delay in the progression of AS with statin medication.(Chan et al., 2010; Cowell et al., 2005; Rossebø et al., 2008)

In addition to statins, several other medical treatments have been evaluated to halt or delay the progression of CAVD. One is antihypertensive strategies to decrease transvalvular pressure gradient by lowering systemic hypertension (Tastet et al., 2017). This strategy is based on the evidence that high transvalvular pressure gradient is observed to promote ECM remodelling of the leaflets by aVICs. Another treatment strategy is Renin-Angiotensin-Aldosterone-System (RAAS)-blocking therapies which also reduce systemic blood pressure, delay LVH development and is documented to have beneficial clinical outcomes in heart failure and reduced ejection fraction (EF) patients (Garg & Yusuf, 1995; Wong et al., 2002). Additionally, RAAS -inhibition attenuates the pro-calcific effects of angiotensin II in calcified valves (O'Brien et al., 2005).

Phosphate and calcium metabolism-targeted therapies are another interesting and potential strategy to delay the progression of AS. Studies have showed that lower bone density is associated with vascular calcification, (Hyder et al., 2009) moreover it was observed that denosumab, a medicine used in osteoporosis, inhibits vascular calcification in pre-clinical studies (Helas et al., 2009). Similar findings have been observed in clinical retrospective studies when analysing bisphosphonate`s effect to AS progression in patients with osteoporosis (Saeed et al., 2012).

Although statins have failed to slow the progression of AS, interest in targeting apolipoprotein B-containing lipoproteins remains high, as elevated levels of these lipoproteins, including Lp(a), have been associated with faster disease progression (Capoulade et al., 2018). Therefore, Lp(a)-lowering strategies have recently emerged as a promising approach to slow the progression of the disease. Examples of Lp(a)-lowering strategies include Proprotein Convertase Subtilisin/Kexin Type 9 inhibitors, niacin medication, antisense oligonucleotide therapy, and RNA interference targeting apolipoprotein(a) (Capelleveen et al., 2016). However, further robust clinical studies are needed to confirm their efficacy and establish evidence-based treatment strategies to delay disease progression and improve patient outcomes. (Marquis-Gravel et al., 2016; Zheng et al., 2020)

Moreover, there is no effective diagnostic tool to identify and monitor the disease progression in patients with early-stage CAVD. This presents a significant challenge for the development of novel medicines. Patients with early-stage CAVD are likely to benefit the most from medical therapy, making it crucial to develop diagnostic tools that can identify this stage of the disease. Such tools would provide the opportunity to evaluate the efficacy of new treatments. CAVD has a dual-part pathophysiology, consisting of early (inflammation and fibrosis) and later (osteogenesis) stages. Additionally, it is observed that calcification is more pronounced in males, whereas females are more likely to develop a fibrotic phenotype of AS. (Lindman & Merryman, 2021) This dual-part and sex-variant pathophysiology presents another challenge when considering novel drug testing.

## 1.2 Management of patients with aortic stenosis

### 1.2.1 Echocardiography and diagnosis of aortic stenosis

Echocardiography is a specialized ultrasound technique used to examine the heart, which provides real-time detailed images and data on its structure and function. The information is displayed as two-dimensional tomographic images or three-dimensional reconstructions. (Leech et al., 2018)

Echocardiography uses high-frequency sound waves to create images of the heart's structures and blood flow. In practice, imaging the heart's structure and studying blood flow are usually imaged and recorded simultaneously, even though there are fundamental differences in these two phenomena. The basic concept of echocardiography closely resembles radar technology, including the type of information gathered and how the information is illustrated. (Leech et al., 2018)

Echocardiography is the first-line diagnostic test to confirm AS and assess the disease severity. Furthermore, it has a crucial role in evaluating obstruction state, LV function and wall thickness, as well as providing prognostic estimates. Echocardiographic assessment of patients with aortic stenosis relies on measurements of the mean pressure gradient, peak transvalvular velocity, and valve area. In unclear situations, additional parameters such as functional status, stroke volume, Doppler velocity index, valve calcification, LV function, LV hypertrophy, flow conditions, and blood pressure control are recommended. Currently there are three broad categories defined to assess severity of the AS.

**Mild AS:** Aortic valve area (AVA) > 1.5 cm², peak transvalvular velocity < 3.0 m/s, and mean pressure gradient < 25 mmHg.

**Moderate AS:** AVA 1.0 – 1.5 cm², peak transvalvular velocity 3.0 – 4.0 m/s, and mean pressure gradient 25 – 40 mmHg.

**Severe AS:** AVA < 1.0 cm², peak transvalvular velocity > 4.0 m/s, and mean pressure gradient > 40 mmHg.

Additionally, new echocardiographic parameters, stress imaging, and non-contrast cardiac computed tomography (CCT) provide valuable information when the severity of the disease is uncertain and aid in planning AVR procedures. The CCT Agatston score quantifies the amount of calcium in the aortic valve. The degree of calcification helps assess stenosis severity and supports clinical decision-making. (Vahanian et al., 2022)

However, both modalities, echocardiography and CCT have limitations in identifying early-stage AS, as these modalities primarily rely on detecting structural and functional changes in the aortic valve rather than providing information about inflammation associated with the disease.

Like in humans, echocardiography for rodents incorporates five main modalities across multiple views and planes: M-mode (motion mode), B-mode (two-dimensional brightness mode), Doppler imaging, speckle-tracking echocardiography, and three- or four-dimensional imaging. (Zacchigna et al., 2021) M-mode, B-mode, and Doppler imaging are used to evaluate the severity of AS and the function of heart. M-mode is primarily used to assess systolic function and LV size, B-mode for EF, fractional shortening, and aortic valve structure, while Doppler imaging is employed to measure blood velocity.

Echocardiography is a non-invasive, reliable, and highly reproducible method for evaluating cardiac function in rodents. The development of echocardiographic devices has successfully facilitated the translation of techniques from humans to rodents, enabling the assessment of disease severity and progression, novel drug testing, and monitoring of cardiac function in genetically modified animals. Additionally, standardized echocardiographic procedures for adult mice have been established (Zacchigna et al., 2021)

### 1.2.2 Molecular imaging

Positron emission tomography (PET) is a non-invasive imaging technique that produces tomographic images based on the distribution of a radionuclide-labelled tracer injected into the body. As a form of molecular imaging, it allows for the visualization, characterization, and measurement of biological processes at the molecular and cellular levels in living subjects. This can provide insights into the pathophysiological processes involved in disease. PET imaging is based on the decay of radionuclides through positron emission. For example, fluorine-18 ($^{18}$F) decays to oxygen-18 ($^{18}$O) and emits a positron ($\beta^+$) and a neutrino ($\nu_e$). (DiFilippo, 2007) (Figure 2)

$$^{18}F \rightarrow {}^{18}O + \beta^+ + \nu_e$$

Neutrinos have no impact on PET imaging. However, the positron, which is considered antimatter, is similar to an electron in terms of mass but has an opposite electrical charge. The positron is emitted from the nucleus and interacts with nearby electrons, losing its kinetic energy. Because positrons and electrons are mutually unstable, they undergo a process known as positron annihilation, where two gamma-ray photons are created. Because the total energy and momentum is conserved each gamma ray has energy of 511 keV, equivalent to mass of the positron and electron, and the two gamma rays travel in opposite directions. (DiFilippo, 2007)

When a pair of 511 keV gamma rays is detected simultaneously and in opposite directions, a line can be drawn from the two detection points to the centre of the scanner. This line helps locate the point in space where the positron emission and annihilation took place. By detecting many such events, the distribution of the positron-emitting radionuclide within the area of interest can be mapped, allowing for the creation of 3D tomographic images. This is the basic principle behind PET imaging. (Figure 2) Because external collimator is not needed to define the angle of detected gamma rays, the limit of spatial resolution in PET imaging is the average distance which the positron travels prior to annihilation (clinical scanners 3-6 mm, pre-clinical scanners 1-2 mm.). However, a disadvantage of PET imaging is its relatively poor anatomic contrast. (DiFilippo, 2007)

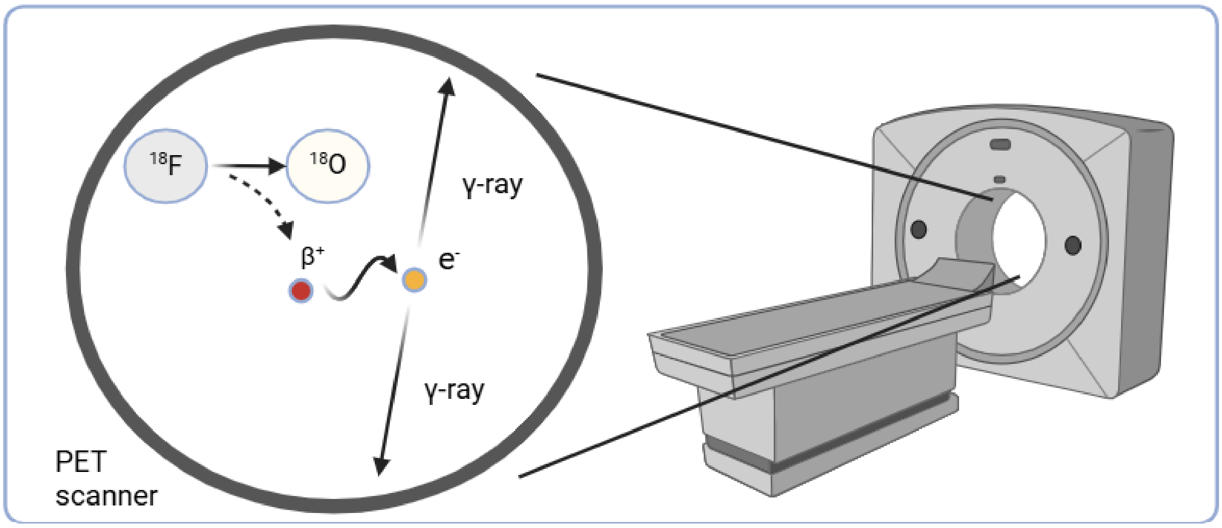

**Figure 2. Radionuclide decay by positron emission and annihilation in PET-imaging.** PET imaging relies on the decay of a radionuclide via positron emission. Following positron annihilation, the positron collides with an electron, resulting two gamma rays. These gamma rays travel in opposite directions and are detected by the PET scanner. Multiple such events are recorded, and their signals are used to reconstruct a 3D tomographic image. *Image created using BioRender.*

Computed tomography (CT) uses a computer to create cross-sectional images of the body, overcoming the limitations of traditional x-ray imaging, where small features are obscured by overlapping structures. In CT, an x-ray tube and detector rotate around the body, capturing x-ray projections from multiple angles to form a slice. These projections are digitally recorded and processed using a computer, which sharpens the images through reconstruction, providing clearer views of internal structures. (Boyd, 2007)

The development of combined PET/CT technology has been an important evolution in the field of imaging. The first PET/CT prototype was developed in 1992, combining CT and PET into single device. CT images are used to correct for attenuation and dispersion in PET emission data, while also providing anatomical references to define tissue boundaries for PET reconstruction. Therefore, combined PET/CT technology provides valuable insights into both the anatomical properties (CT) and functional properties (PET) of the structure of interest, overcoming the major limitation of PET, poor anatomic contrast. (Townsend et al., 2007)

Sodium fluoride (NaF) is one the oldest radiopharmaceuticals for bone imaging, initially with conventional γ-cameras and, since the 1990s, with PET scanners (Ahuja et al., 2020). In addition to bone imaging, fluorine-18-labelled NaF ($^{18}$F-NaF) has been shown to provide valuable information on calcification processes in vascular tissues (Tzolos & Dweck, 2020).

Similarly, as hydroxyapatite have a crucial role in bone remodelling, it is also a key component of vascular calcification (Villa-Bellosta, 2021). Therefore, $^{18}$F-NaF has been investigated as a radiotracer to image CAVD and atherosclerosis. $^{18}$F-NaF uptake has been demonstrated in several studies to detect microcalcification in the aortic valves of patients with AS (Dweck et al., 2014; Pawade et al., 2016; Zheng et al., 2019). Moreover, increased $^{18}$F-NaF uptake can predict the development and progression of aortic valve calcification and AS (Dweck et al., 2014; Jenkins et al., 2015, p. 18).

Another radiotracer used to study disease processes in the cardiovascular system is the glucose analog 2-deoxy-2-[$^{18}$F]-fluoro-D-glucose ($^{18}$F-FDG). This tracer is taken up by metabolically active cells via glucose transporters, but it cannot continue through the glycolytic pathway and instead accumulates inside the cells. This accumulation allows real-time imaging of tissue metabolic activity. $^{18}$F-FDG has been used to detect cardiac inflammation (Blankstein et al., 2014) and inflammation in atherosclerotic lesions due to the high glucose consumption by macrophages during inflammation (Dweck et al., 2016). In patients with aortic stenosis, increased $^{18}$F-FDG uptake in the valve has been observed, although interpretation can be challenging due to high physiological tracer uptake in the surrounding myocardium (Abdelbaky et al., 2015). Thus, there is growing interest in using PET as a marker of disease activity to detect AS in a stage when valvular calcification is more likely to be reversible.

## 1.3 Macrophages and folate receptor-β (FR-β)

### 1.3.1 Nature of macrophages

The mononuclear phagocyte system consists of immune cells originating from bone marrow myeloid progenitors, including monocytes, macrophages, and dendritic cells. These cells are responsible for in phagocytosis, antigen presentation, and cytokine production. (Peet et al., 2020) These immune cells develop in the bone marrow and are released into the bloodstream, where they are categorized into two main types based on their function and surface markers, classical and non-classical monocytes. Monocytes are short-lived circulating cells involved in inflammation directly and by differentiating into dendritic cells and macrophages. (Ingersoll et al., 2010)

As monocytes enter tissues, they differentiate into dendritic cells and macrophages. Macrophages differ from monocytes by having increased expression of cluster of differentiation (CD)68 and reduced expression of CD14 in humans, and by increased expression F4/80 in mice. Macrophages are involved in multiple processes, including cytokine production, phagocytosis, coordination of repair and healing during inflammation, and maintaining homeostasis in specific organs. (Peet et al., 2020)

Macrophages have historically been divided into two subtypes: classically activated pro-inflammatory macrophages (M1) and alternatively activated anti-inflammatory macrophages (M2). Although the M1/M2 classification is not comprehensive, as macrophages can adopt mixed phenotypes, exhibit bipolar activation, or have subtypes outside this framework, it has been useful in explaining the complex characteristics of macrophages. (Skytthe et al., 2020)

In addition to macrophages recruited from the bone marrow, recent studies have revealed new insights into tissue-resident macrophages and their role in maintaining heart valve ECM homeostasis (Kim et al., 2020). Resident macrophages originate during embryonic development and continue to perform immune and homeostatic surveillance functions into adulthood. It is estimated that at least 75% of the immune cells located in heart valves express macrophage markers, encompassing both resident and recruited populations (Hulin et al., 2019). The specific functions of these resident macrophages are still largely unknown, though they are involved in maintaining valve integrity, ECM remodelling, aging and disease progression in various contexts (Kim et al., 2020; Shigeta et al., 2019).

Metabolic stress, ischemia, or trauma can lead to cell injury and the release of Danger-Associated Molecular Patterns (DAMPs). DAMPs are molecules released from damaged or dying cells, which trigger an immune response and promote further tissue damage (Long et al., 2023). These molecules activate the innate immune system through pattern recognition receptors, leading to release of multiple pro-inflammatory mediators. Resident macrophages are crucial components of the innate immune system, serving as the initial defence against pathogens (Long et al., 2023). Pro-inflammatory cytokines released by innate immune cells, along with lipid mediators, induce the M1 macrophage phenotype. Moreover, M1 macrophages create an inflammatory microenvironment by releasing pro-inflammatory mediators, which can trigger different types of cell death. (Lech & Anders, 2013).

In context of tissue injury, repair, healing, and homeostasis, M2 macrophages can be categorized into three subtypes based on their functionality and phenotype (Long et al., 2023). M2a macrophages are activated by IL-4 and IL-13, and they secrete IL-10, IL-1 receptor antagonists, and growth factors that promote tissue healing and exhibit anti-inflammatory effects. Additionally, M2a macrophages are strongly associated with wound healing and tissue fibrosis. M2b macrophages contribute to anti-inflammatory responses by secreting IL-10. However, they also have immunomodulatory effects through interactions with Type 2 T-helper cells, which are not exclusively anti-inflammatory. The third subtype, M2c macrophages, is activated by factors such as IL-10, transforming growth factor-β (TGF-β), and glucocorticoids. These stimuli drive the proliferation of M2c macrophages, enhancing their roles in tissue repair and the suppression of tissue inflammation. (Long et al., 2023)

Although M2 macrophage activation is generally considered beneficial in tissue injuries due to its ability to suppress focal inflammation and enhance tissue repair, it can become problematic in tissues with limited regenerative capacity, like the heart. Because of the heart's limited ability to regenerate, it undergoes a rapid healing process that prioritizes scar formation, which can compromise its functionality (Long et al., 2023). M2 macrophages are involved in fibrotic processes by actively secreting a wide range of pro-fibrotic factors, such as transforming growth factor-β1, fibroblast growth factor 2, and galectin-3. These factors promote myofibroblast proliferation and activation, leading to excessive production of ECM components. Moreover, macrophages secrete cytokines that trigger EndMT, further enhancing ECM remodelling. (Braga et al., 2015)

### 1.3.2 Macrophage FR-β as an imaging target

Folate, also known as vitamin B9, is critical for nucleotide synthesis by providing the necessary methyl groups for DNA and RNA production. Because folate is a hydrophilic anionic molecule, it does not cross membranes by simple diffusion and instead requires transport system to facilitate its entry into cells. For this reason, folate is transported into the cell via two main mechanisms. One pathway uses a transmembrane transport protein known as the reduced folate carrier, while the other depends on the proton-coupled folate transporter, which enables the bidirectional transfer of folate. (Matherly & Goldman, 2003)

Folate can be internalized by the folate receptor, enabling unidirectional transport into the cells. FR-β is one of the two glycosyl-phosphatidylinositol-anchored membrane-bound folate-binding proteins, and the other is folate receptor alpha (FR-α). FR-α is more commonly associated with cancer cells, while FR-β is present on activated macrophages. It has been observed that FR-β is highly expressed on activated macrophages but not in resting macrophages and monocytes at the site of inflammation. (Lu et al., 2021)

FR-β expression has been identified in various inflammatory conditions, such as rheumatoid arthritis, Crohn's disease, pulmonary disease, psoriasis, sarcoidosis, atherosclerosis, and myocardial infarction. (Paulos et al., 2004). Recently, a radiolabelled folate derivative has been successfully used for PET imaging of inflammation in atherosclerotic plaques (Silvola et al., 2018) and autoimmune myocarditis (Jahandideh et al., 2020). However, the potential of FR-β-targeted PET imaging has not yet been explored in CAVD.

Folate -based PET imaging tracer aluminium $^{18}$F-labeled 1,4,7-triazacyclononane-*N, N', N''*-triacetic acid (NOTA)-conjugated folate (Al$^{18}$F-NOTA-folate or shortly $^{18}$F-FOL) is produced by incubating [$^{18}$F]-fluoride with aluminium chloride ($AlCl_3$) and heating it in the presence of NOTA-folate. This procedure has been demonstrated to produce $^{18}$F-FOL with high molar activity and radiochemical purity. (Silvola et al., 2018)

*In vivo* stability of $^{18}$F-FOL has been tested in mice and rabbits, showing that 85% of the tracer remains intact 60 minutes post-injection. The translational potential of $^{18}$F-FOL has also been demonstrated using ischemic human carotid endarterectomy sections in vitro, where clear colocalization was observed between $^{18}$F-FOL binding and macrophages positive to FR-β and CD68. Additionally, the specificity of $^{18}$F-FOL binding to FR has been demonstrated *in vitro* assays. Significantly lower binding was observed when folate glucosamine was used for incubation, effectively blocking the binding. (Silvola et al., 2018)

Moreover, Jahandideh et al. (2020) demonstrated specific uptake of $^{18}$F-FOL in inflamed myocardium containing macrophages expressing FR-β. They also highlighted the translational potential of $^{18}$F-FOL by showing FR-β expression in human cardiac sarcoidosis lesions. Additionally, they demonstrated that $^{18}$F-FOL is specific towards inflamed myocardium in rats and observed a predominance of CD68-positive macrophages, including both M1- and M2-polarized types.

## 1.4 Aims and hypotheses

Macrophages are key contributors to the progression of CAVD by driving inflammatory, pro-fibrotic, and pro-calcific processes within the valve leaflets. It has been demonstrated that FR-β is expressed on activated macrophages, but not on resting macrophages or monocytes. Based on these observations, we hypothesize that the expression of FR-β is increased in the aortic valve during inflammatory and fibro-calcific processes associated with CAVD, making it a potential target for detecting the active initiation phase of CAVD via PET/CT imaging using an FR-β-targeted radionuclide tracer. The specific aim of this study is to evaluate the feasibility of a PET tracer $Al^{18}F$-NOTA-folate for the detection and imaging of inflammation in experimental CAVD.

# 2 Results

A total of 16 mice were divided equally into two groups: CAVD (n = 8) and control (n = 8). The mean age of the CAVD group was 12.7 ± 0.7 months, while the mean age of the control group was 12.9 ± 0.4 months.

Both groups underwent echocardiography and PET/CT imaging using $^{18}$F-NaF and Al$^{18}$F-NOTA-folate tracers. Following imaging, ex vivo biodistribution, autoradiography, and immunohistochemical analyses were performed.

At the end of the study, a statistically significant difference in weight was observed between the groups. The CAVD group had a mean weight of 37.2 ± 5.9 g, while the control group had a mean weight of 43.7 ± 4.9 g ($p = 0.041$). Non-fasting blood glucose levels were monitored before Al$^{18}$F-NOTA-folate imaging, with no significant difference observed between the groups: 8.8 ± 1.6 mmol/L in the CAVD group vs. 9.6 ± 0.9 mmol/L in the control group ($p = 0.295$)

## 2.1 Echocardiography

In echocardiography, the following parameters were assessed: transvalvular peak flow velocity (mm/s), and peak gradient (mmHg), ejection fraction (EF), left ventricular diastolic volume indexed [LVDvol(i)] (µL/g), and left ventricular systolic volume indexed [LVSvol(i)]. transaortic peak flow velocity and peak gradient were measured to detect possible aortic stenosis, while EF, LVDvol(i), and LVSvol(i) were evaluated to assess potential functional changes in the heart.

Doppler imaging was employed to assess transvalvular peak flow velocity and peak gradient (Figure 3A), while B-mode imaging was used to assess EF, LVDvol(i), and LVSvol(i) (Figure 3B). Importantly, no significant difference in heart rate was observed during echocardiographic imaging between the groups, with values of 480 ± 72 beats/min in the CAVD group and 480 ± 26 beats/min in the control group.

Transvalvular peak flow velocity was significantly higher in CAVD mice, with a mean of 1400 ± 250 mm/s, compared to 640 ± 210 mm/s in controls ($p < 0.0001$) (Figure 3F). Similarly, peak gradient was significantly elevated in the CAVD group (8.0 ± 2.6 mmHg) versus the control group (1.8 ± 1.3mmHg) ($p < 0.0001$) (Figure 3G). These findings indicate the presence of hemodynamically significant aortic stenosis in CAVD mice.

The mean LVDvol(i) was 1.7 ± 0.32 μL/g in the CAVD group and 1.4 ± 0.31 μL/g in the control group, with no statistically significant difference between the groups ($p = 0.194$) (Figure 3C). In contrast, LVSvol(i) was significantly elevated in CAVD mice compared to controls ($p = 0.012$), with mean values of 0.77 ± 0.14 μL/g and 0.57 ± 0.11 μL/g, respectively (Figure 3D). Significant difference was also found in EF ($p = 0.004$), with values of 53.0 ± 4.8 % in the CAVD group and 60 ± 2.3 % in the control group (Figure 3E), indicating altered cardiac function and possible hypertrophy in the CAVD group. One control mouse was excluded from EF, LVDvol(i), and LVSvol(i) analyses due to the inability to reliably define LV endocardial borders.

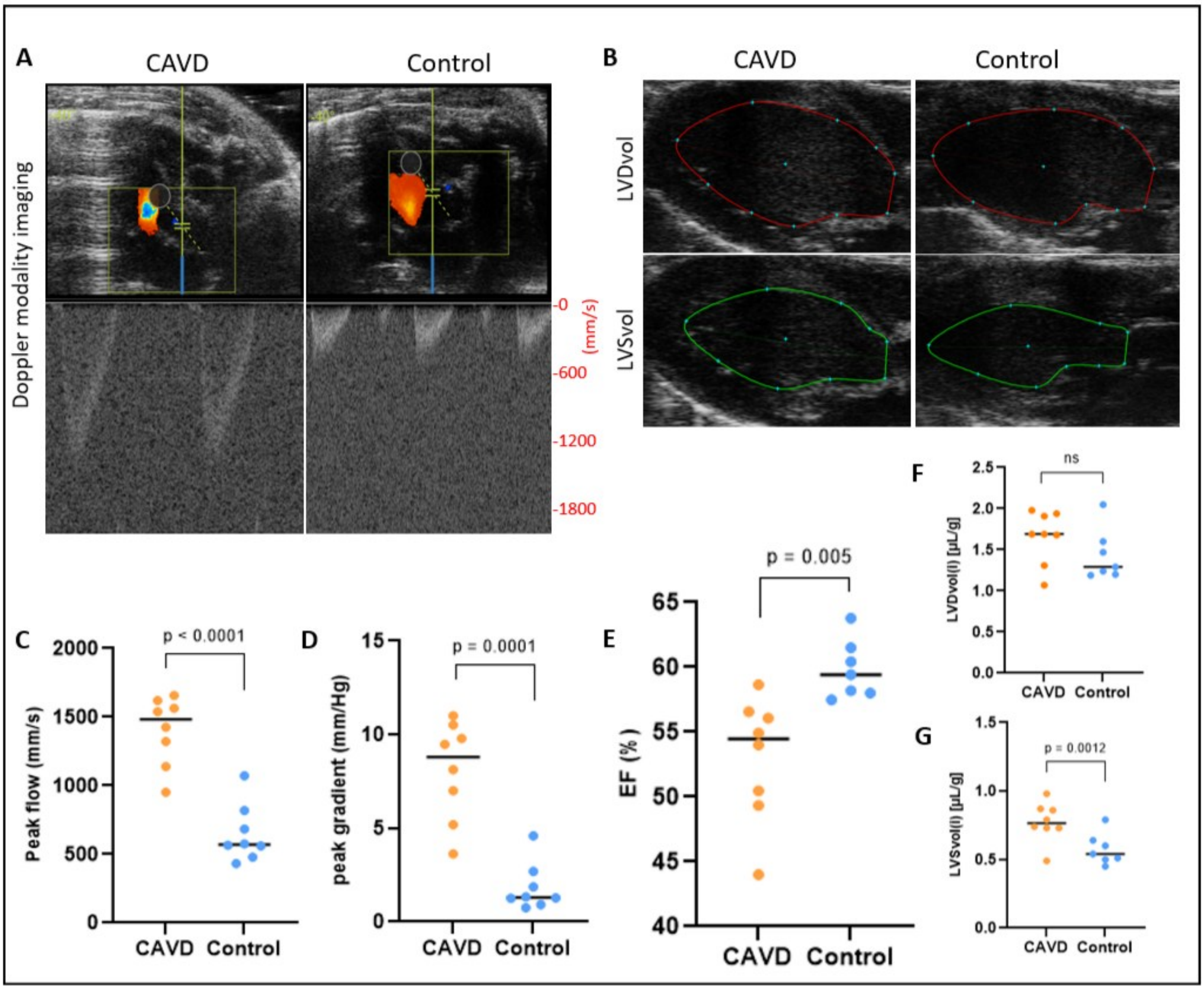

**Figure 3. Echocardiography of left ventricular function and aortic flow. (A)** Doppler modality images showing transaortic peak flow velocity and peak gradient measurements. **(B)** B-mode long-axis images illustrating left ventricular function assessment in CAVD and control mice where lines represent endocardial borders. **(C–G)** Quantitative comparison of key echocardiographic parameters between CAVD and control groups: **(C)** transaortic peak velocity **(D)** peak transaortic gradient, **(E)** Ejection

fraction (EF), **(F)** left ventricular diastolic volume index [LVDvol(i)], and **(G)** left ventricular systolic volume index [LVSvol(i)]. Data are presented as mean (black line) with individual values. Group comparisons were analysed using an unpaired t-test, and peak gradient and EF with Welch`s t-test.

## 2.2 In vivo PET/CT imaging and biodistribution

Figure 4 illustrates the uptake of Al$^{18}$F-NOTA-folate in the aortic valve, showing clear tracer accumulation in this region at 50–60 minutes post-injection (indicated by arrows). In contrast, no detectable uptake was observed in the healthy aortic valves of control mice. Data analysis revealed significantly higher valvular uptake in CAVD mice, with SUV$_{mean}$ 0.56 ± 0.07 compared to 0.36 ± 0.06 in the control group ($p < 0.0001$) (Figure 4A)

Moreover, the target-to-background (TBR) (SUV$_{mean}$, valve/SUV$_{mean}$, blood) was significantly higher in the CAVD group compared to the control group: 1.9 ± 0.32 vs. 1.1 ± 0.07 ($p < 0.0001$) (Figure 4B). No significant difference in blood (LV) uptake, which was used as the background, was observed between the groups: 0.31 ± 0.08 in the CAVD group vs. 0.31 ± 0.06 in the control group ($p > 0.05$).

Furthermore, $^{18}$F-NaF uptake was observed in the aortic valve region of the CAVD group, whereas no uptake was detected in the control group (Figure 4). A statistically significant difference was found in the SUV$_{mean}$ (50–60 min) between the groups: 0.64 ± 0.23 in the CAVD group vs. 0.40 ± 0.05 in the control group ($p = 0.011$) (Figure 4C). The TBR was also significantly higher in the CAVD group compared to the control group: 1.8 ± 0.47 vs. 1.1 ± 0.22 ($p < 0.001$) (Figure 4D). Lastly, no difference in blood (LV) SUV$_{mean}$ was observed ($p = 0.882$): 0.35 ± 0.08 in the CAVD group vs. 0.39 ± 0.10 in the control group.

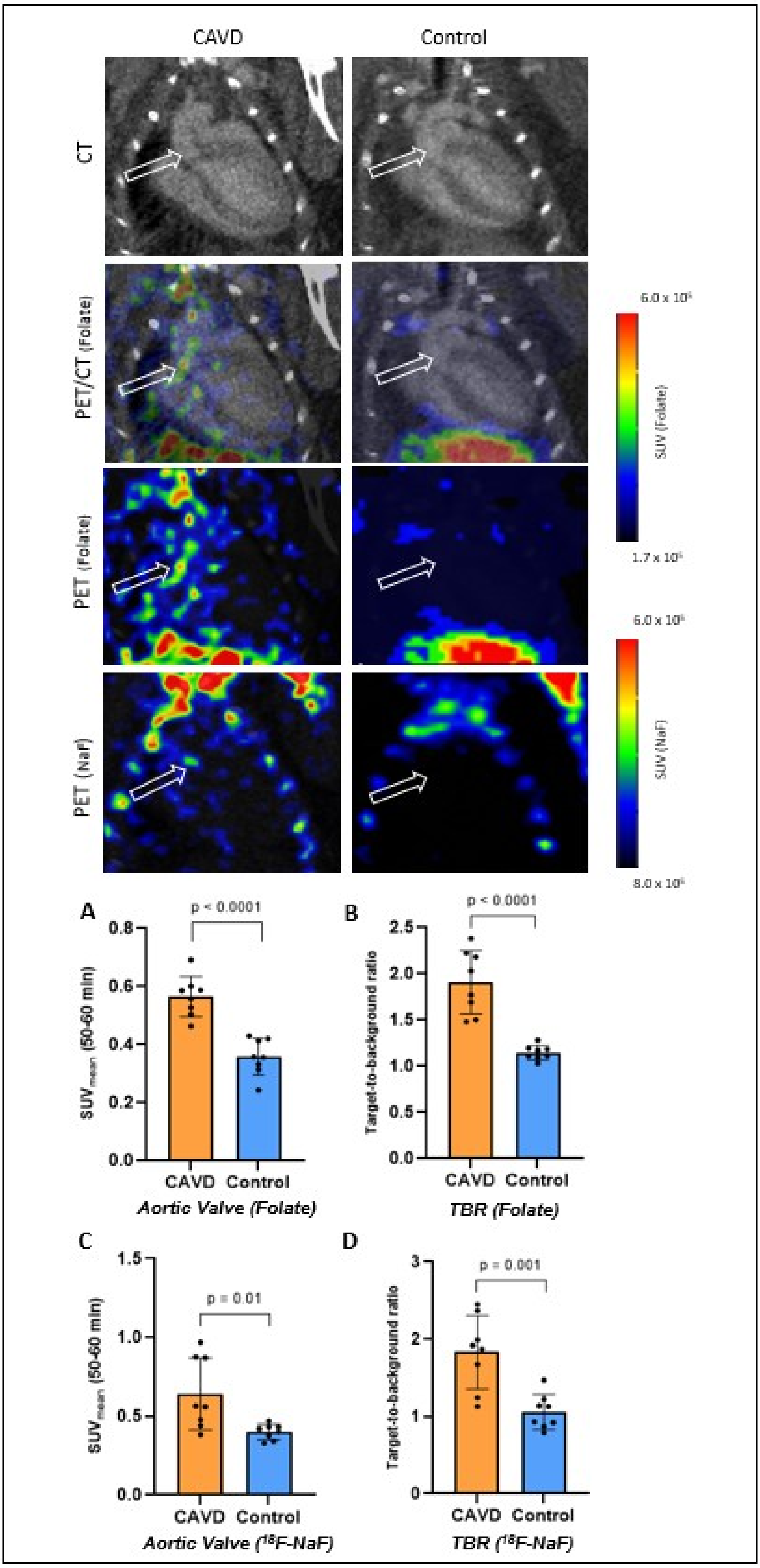
CAVD
Control
CT
PET/CT (Folate)
PET (Folate)
PET (NaF)
$6.0 \times 10^5$
SUV (Folate)
$1.7 \times 10^5$
$6.0 \times 10^5$
SUV (NaF)
$8.0 \times 10^5$
A
p < 0.0001
0.8
0.6
0.4
0.2
0.0
$SUV_{mean}$ (50-60 min)
CAVD
Control
Aortic Valve (Folate)
B
p < 0.0001
2.5
2.0
1.5
1.0
0.5
0.0
Target-to-background ratio
CAVD
Control
TBR (Folate)
C
1.5
1.0
0.5
0.0
p = 0.01
$SUV_{mean}$ (50-60 min)
CAVD
Control
Aortic Valve ($^{18}$F-NaF)
D
3
2
1
0
p = 0.001
Target-to-background ratio
CAVD
Control
TBR ($^{18}$F-NaF)

**Figure 4. $Al^{18}F$-NOTA-folate and $^{18}F$-NaF PET/CT Imaging.** Representative PET/CT images and quantitative analysis of $Al^{18}F$-NOTA-folate and $^{18}F$-NaF uptake in aortic valve region. Contrast-enhanced CT and PET/CT images show tracer uptake in the aortic valve region, indicated by arrows. $Al^{18}F$-NOTA-folate PET reflects increased folate receptor expression in activated macrophages, while $^{18}F$-NaF PET highlights areas of microcalcification in CAVD mice. Quantification of tracer uptake is illustrated in bottom panels. **(A)** $SUV_{mean}$ in the aortic valve, and **(B)** Valve-to-blood (TBR), for $^{18}F$-NOTA-folate imaging. **(C and D)** show the same parameters for $^{18}F$-NaF imaging. CAVD mice showed significantly higher tracer uptake ($p < 0.05$) in aortic valve region compared to controls. The PET colour scale represents standardized uptake values (SUV), with red/yellow indicating higher tracer accumulation.

To assess the whole body biodistribution of $Al^{18}F$-NOTA-folate at 50-60 minutes post injection and to compare uptake differences between groups, additional regions of interest (ROIs) were drawn. The results are summarized in Table 1 (*In vivo*). Overall, $Al^{18}F$-NOTA-folate was rapidly cleared from body and excreted in the urine in both groups. The highest uptake was observed in the liver and in kidneys. Data analysis revealed a statistically significant difference in the $SUV_{mean}$ of the aortic arch, indicating atherosclerotic lesions, lungs, and kidney. In contrast, no significant differences were observed in blood, myocardium, liver, sternum, spleen, or urine $SUV_{mean}$ between the groups.

*Ex vivo* biodistribution analysis was conducted immediately after $Al^{18}F$-NOTA-folate PET/CT imaging to gain further insight into the tracer's metabolic nature and to provide supportive evidence for those tissues which were challenging to draw ROIs in PET/CT images (Table 1, *Ex vivo*). Results were also expressed as SUVs, normalized to the injected radioactive dose, animal body weight, and tissue weight. Significant difference was observed in tracer accumulation between the groups in the small intestine, whereas difference in cortical bone, bone marrow, pancreas and white adipose tissue was not observed.

**Table 1. *In vivo & ex vivo* Biodistribution of Al$^{18}$F-NOTA-folate.**

| ***In vivo***<br>Tissue | CAVD | Control | *p* -value |
|---|---|---|---|
| Blood (LV) | 0.31 (0.08) | 0.31 (0.06) | *0.88* |
| Aortic arch | 0.61 (0,15) | 0.46 (0,10) | 0.02 |
| Myocardium | 0.29 (0.06) | 0.38 (0.09) | 0.05 |
| Liver | 1.7 (0.30) | 2.4 (1.1) | 0.14 |
| Lungs | 0.28 (0.04) | 0.42 (0.11) | 0.01 |
| Sternum | 0.39 (0.11) | 0.41 (0.09) | 0.72 |
| Spleen | 0.58 (0.18) | 0.53 (0.18) | 0.61 |
| Kidney | 15 (2.3) | 22 (3.7) | < 0.001 |
| Urine | 81 (42) | 38 (28) | 0.27 |

| ***Ex vivo***<br>*Tissue* | CAVD | Control | *p* -value |
|---|---|---|---|
| Cortical bone | 0.12 (0.27) | 0.17 (0.11) | *0.9* |
| Bone marrow | 0.101 (0.02) | 0.08 (0.02) | 0.16 |
| Small intestine | 0.63 (0.28) | 1.2 (0.51) | *0.02* |
| Pancreas | 0.23 (0.06) | 0.31 (0.10) | *0.14* |
| White adipose tissue | 0.18 (0.06) | 0.20 (0.05) | 0.36 |

All results are presented as $SUV_{mean}$ and standard deviation (SD). Comparisons of unpaired data between the two groups were conducted using the t-test, assuming similar SDs between the groups. A p-value of less than 0.05 was considered statistically significant.

## 2.3 Autoradiography

Histological analysis using H&E (haematoxylin and eosin) staining and autoradiography of cross-sections of the aortic valve in both the CAVD and control groups is illustrated in Figure 6A. The scale bar represents photo-stimulated luminescence (PSL/mm²), where yellow/red indicates higher luminescence and green/blue indicates lower luminescence, reflecting the uptake of the tracer. The uptake of $Al^{18}F$-NOTA-folate was measured in the following ROIs: aortic plaques, aortic valve leaflets, and the myocardium near the aortic root. ROIs were drawn in approximately five different cross-sections of the aortic valve.

In the H&E images of the CAVD group, extensive plaque formation was observed within the aorta (marked with a triangle). This plaque formation corresponds to strong red coloration in the autoradiography image, indicating high $Al^{18}F$-NOTA-folate accumulation. The mean uptake in atherosclerotic plaques of the CAVD group was 260 ± 100 PSL/mm² (Figure 6B). In contrast, no plaque formation was observed in the control group. Additionally, yellow coloration is seen in the aortic leaflets of the CAVD group's autoradiography image, whereas blue coloration is predominant in the same region in the control group (marked with an arrow).

However, no statistically significant difference was found in the mean PSL/mm² values of the aortic valve leaflets between the groups: 100 ± 38 PSL/mm² in the CAVD group and 91 ± 33 PSL/mm² in the control group ($p = 0.591$) (Figure 6B). Similarly, no significant difference was observed in PSL/mm² values in the myocardium between the groups: 44 ± 17 PSL/mm² in the CAVD group and 52 ± 17 PSL/mm² in the control group ($p = 0.632$) (Figure 6B, marked with red circle).

Interestingly, when PSL/mm² values of the aortic valve leaflets were normalized to those of the myocardium, a statistically significant difference was observed ($p = 0.0098$): 2.4 ± 0.47 in the CAVD group compared to 1.7 ± 0.27 in the control group (Figure 6B).

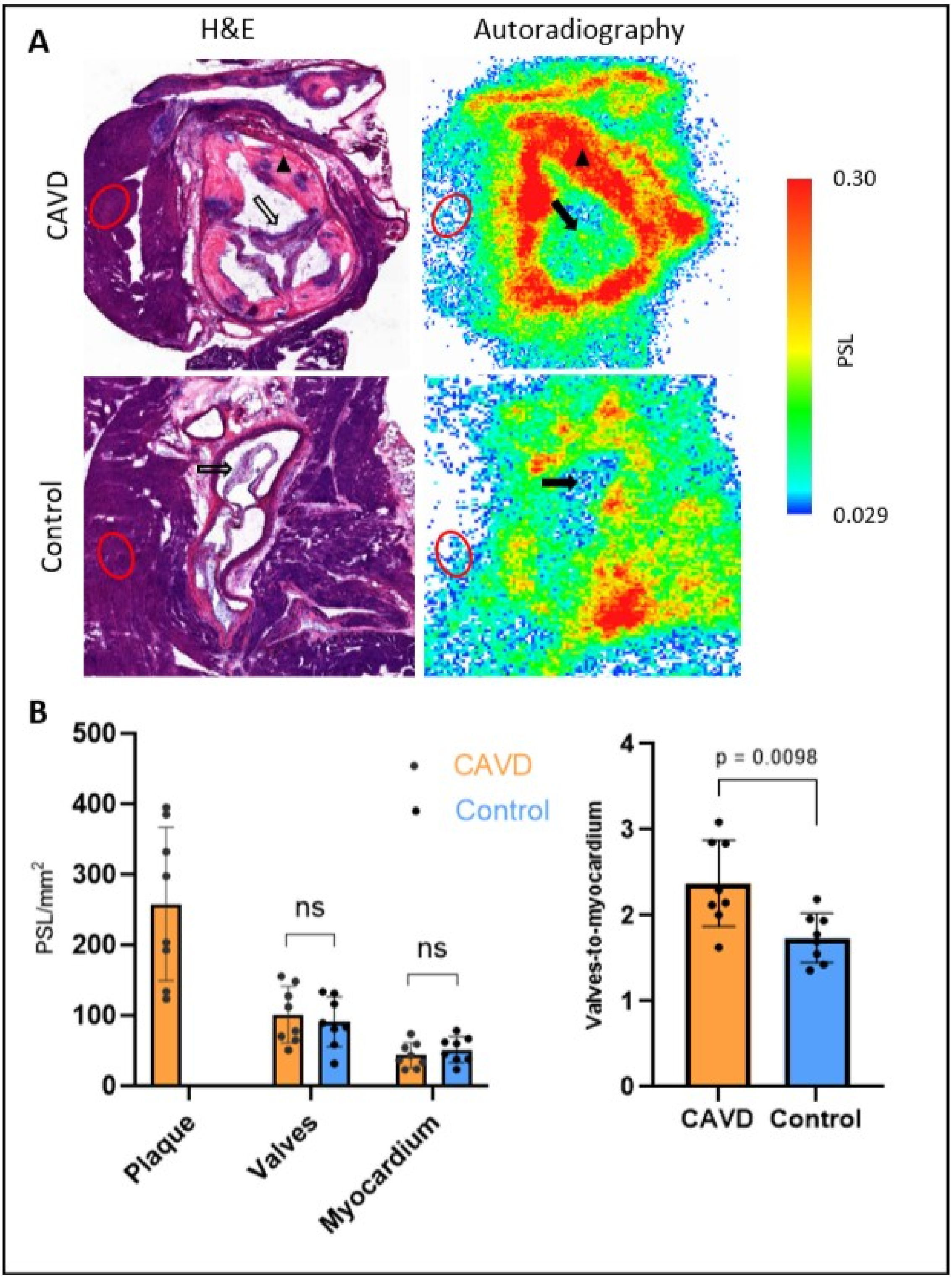

**Figure 6. Autoradiography analyses of Al$^{18}$F-NOTA-folate.** To assess the uptake of Al$^{18}$F-NOTA-folate in the aortic valves, cryosections from the aortic root of CAVD and healthy mouse models were analysed. H&E and autoradiography (ARG) images were merged, and uptake was quantified in three regions of interest (ROIs): aortic plaques marked with a triangle, aortic valve leaflets marked with an arrow, and the myocardium near the aortic root marked with a red circle **(Panel A)**. Group comparisons were conducted using unpaired t-tests and valves-to-myocardium with Welch's t-tests, and results are expressed as mean PSL/mm² ± SD. No statistically significant difference was observed in the mean PSL/mm² values of the aortic valve leaflets between groups ($p = 0.59$) (Panel B). However, the valve-to-myocardium PSL ratio was significantly higher in the CAVD group compared to controls ($p = 0.0098$) **(Panel B)**.

## 2.4 Immunohistochemical staining

Immunohistochemical analyses were performed on 8-µm cryosections of the aortic root. Two different staining methods were utilized: Mac-3 to evaluate macrophage presence and Alizarin Red S to identify calcium deposits. While Mac-3 staining was analysed quantitatively, calcium deposits were assessed qualitatively.

In histological analyses thickening of aortic valves was observed in CAVD mice when comparing to control groups. In Mac-3-stained sections, positively stained areas (brown areas marked with a red circle) were observed within the leaflets in both groups, indicating the presence of macrophages (Figure 7A). Moreover, larger and continuous Mac-3 positive areas were detected in CAVD group whereas similar observation was not confirmed in control group mice. Additionally, dark black regions were detected inside the leaflets in both groups which are most likely melanin pigment produced by valvular cells rather than macrophages (marked with a black arrow).

Quantitative analysis revealed a significant difference in leaflet area between the groups ($p = 0.036$), with an average of $0.26 \pm 0.06$ mm$^2$ in the CAVD group compared to $0.18 \pm 0.06$ mm$^2$ in the control group. Similarly, the absolute Mac-3-stained area was significantly larger in the CAVD group ($p = 0.018$), measuring $0.06 \pm 0.02$ mm$^2$ vs. $0.04 \pm 0.01$ mm$^2$ in controls. However, when Mac-3-stained area was normalized to the total valve area, no significant difference was found between the groups: $21.36 \pm 3.26$ % in CAVD vs. $19.70 \pm 3.38$ % in controls ($p = 0.366$). (Figure 7B)

In Alizarin Red S-stained sections, small, red-stained areas were detected inside the leaflets of the CAVD group, indicating calcium deposition (marked with a red arrow in Figure 7A). These deposits were absent in the control group. In all individuals from the CAVD group, calcium accumulation was primarily observed at the leaflet insertions. However, large, calcified areas were not present inside the leaflets. In two cases, isolated calcium deposits were also identified in the central leaflet regions. Additionally, heavy calcium accumulation was observed inside the plaque formations (marked with a black asterisk).

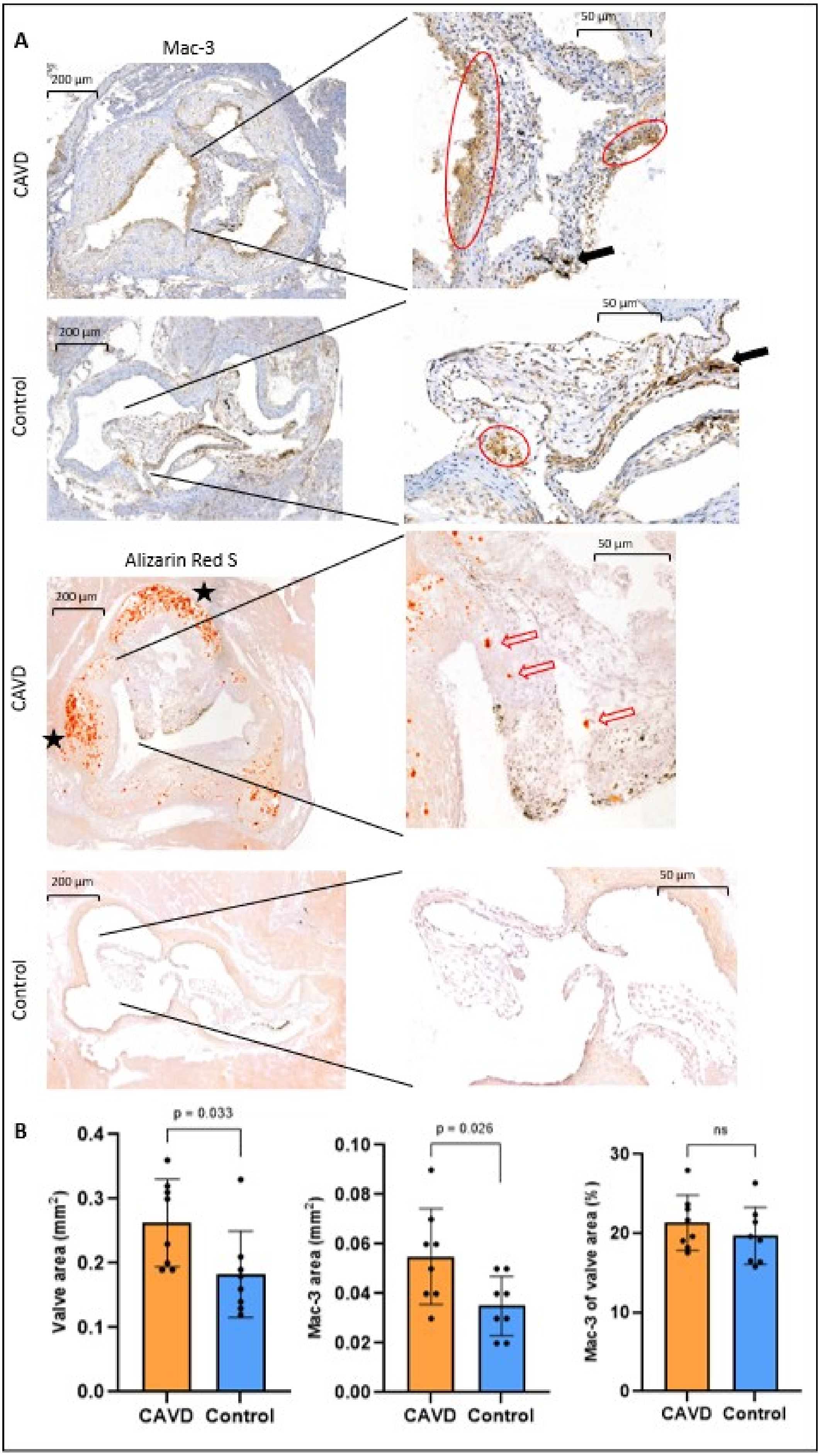
A
Mac-3
CAVD
Control
200 µm
50 µm
Alizarin Red S
CAVD
Control
B
p = 0.033
Valve area (mm$^2$)
0.4
0.3
0.2
0.1
0.0
CAVD
Control
p = 0.026
Mac-3 area (mm$^2$)
0.10
0.08
0.06
0.04
0.02
0.00
CAVD
Control
ns
Mac-3 of valve area (%)
30
20
10
0
CAVD
Control

**Figure 7. Immunohistochemical staining of aortic valve sections. (A)** Representative Mac-3- and Alizarin Red S-stained aortic valve cryosections with higher-magnification images from the CAVD and control groups. Mac-3 staining (brown areas, red circles) highlights macrophage presence in both groups, with larger contiguous stained regions observed in CAVD. Dark black regions (black arrows) likely represent melanin pigment. Alizarin Red S staining reveals small calcium deposits (red arrows) within the CAVD leaflets and heavy calcium accumulation in plaque, whereas no deposits were detected in controls. In the CAVD group, macrophage accumulation appears more extensive, and calcium deposits are primarily located near leaflet insertions. However, no large, calcified areas were observed. **(B)** Quantitative comparison of Mac-3 staining and valve morphology between the CAVD and control groups. **Left:** Valve area (mm²) was significantly larger in the CAVD group ($p = 0.033$). **Middle:** Absolute Mac-3-stained area (mm²) was also significantly increased in the CAVD group ($p = 0.026$). **Right:** When normalized to total valve area, Mac-3 staining percentage did not significantly differ between groups (ns = not significant). *Data are shown as mean ± SD, with individual data points.*

## 2.5 Correlations of echocardiography and Al$^{18}$F-NOTA-folate uptake with histological findings

Several correlation analyses were conducted to examine the association between aortic stenosis, Al$^{18}$F-NOTA-folate uptake, and histological findings. Correlations were analysed in both groups. In the echocardiography analyses, one mouse from the CAVD group was excluded due to LVH, which significantly reduced peak transvalvular flow velocity.

A strong positive correlation was observed between immunohistochemical staining and peak velocity in echocardiography, with $r = 0.842$, $p = 0.022$ in the CAVD group and $r = 0.648$, $p = 0.083$ in the control group (Figure 8A). When comparing aortic valve Al$^{18}$F-NOTA-folate uptake with echocardiographic findings, a moderate correlation was observed between the aortic valve SUV$_{mean}$ and peak velocity (mm/s) in the CAVD group ($r = 0.432$, $p = 0.341$), whereas no similar correlation was found in the control group ($r = -0.131$, $p = 0.759$) (Figure 8B). However, no correlation was observed between aortic valve Al$^{18}$F-NOTA-folate uptake and immunohistochemical analyses in either the CAVD ($r = -0.128$, $p = 0.781$) or control group ($r = -0.103$, $p = 0.819$) (Figure 8C).

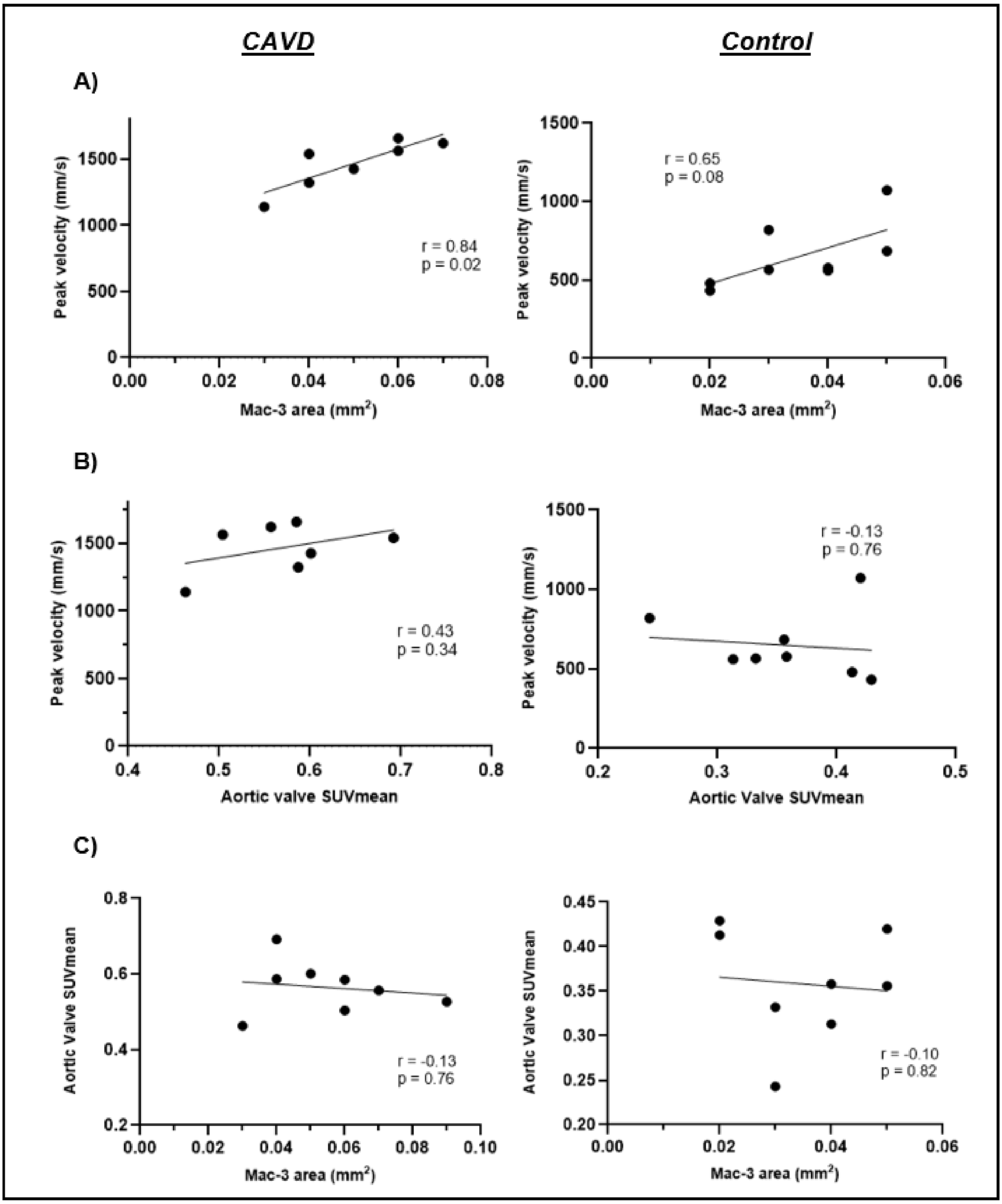

**Figure 8. Correlations between PET, echocardiography, and immunohistochemical stainings.** Correlations were analysed in both the CAVD and control groups. **A)** A strong correlation was observed between immunoassays and echocardiographic measurements in both groups. **B)** In the CAVD group, a moderate correlation was found between the aortic valve SUVmean in Al$^{18}$F-NOTA-folate PET and the peak transvalvular velocity (mm/s) in echocardiography, whereas no correlation was observed in the control group. **C)** No correlation was found between the Mac3-positive area (mm²) and the aortic valve SUVmean in either the CAVD or control groups. All correlations were analysed using Pearson's test, as all variables followed a normal distribution. A p-value < 0.05 was considered statistically significant.

# 3 Discussion

The increasing prevalence of CAVD in the aging population presents a significant healthcare challenge (Pawade et al., 2015). Despite being the most common type of valve disease, there are currently no effective medical treatments to stop or delay its progression (Otto et al., 2021). Moreover, the high risk of heart failure even after successful AVR, along with the failure of statins and other therapies to slow AS progression (Lindman et al., 2021), underscores the need for earlier intervention, novel diagnostics, and improved therapeutic strategies (Roth et al., 2020). Given the progressive nature of CAVD, earlier intervention could lead to more effective treatment outcomes. This study aimed, at least in part, to address these challenges by exploring whether PET imaging could detect inflammation associated with the early phase of CAVD.

In our study echocardiography demonstrated hemodynamically significant AS in CAVD mice compared to healthy controls. Both $^{18}$F-NaF and Al$^{18}$F-NOTA-folate PET imaging revealed significant visual and quantitative differences between the groups. Although autoradiography showed no significant differences in PSL/mm² values of aortic leaflets, normalization to myocardium revealed a significant difference. Furthermore, immunohistochemical analysis demonstrated larger, more continuous Mac-3-positive areas in the CAVD group compared to controls.

In the following sections, these results and their significance will be examined in more detail from various perspectives. Additionally, we will look ahead and consider what aspects should be studied next to gain a deeper understanding of CAVD, the associated inflammation, and its imaging possibilities.

## 3.1 Development of aortic stenosis in CAVD mice

In echocardiographic analyses, the CAVD group exhibited significantly higher peak transvalvular flow velocity and peak gradient compared to the control group. Moreover, we observed significant differences in LVSvol(i) and EF, with the CAVD group showing a higher LVSvol(i) and a reduced EF. However, no significant difference was found in LVDvol(i) between the groups, although in two cases, a clearly reduced diastolic volume was observed, suggesting possible LV hypertrophy.

These findings suggest that mice in the CAVD group likely developed hemodynamically significant aortic stenosis, leading to LV dysfunction, as indicated by the increased LVSvol(i) and reduced EF. However, since LVDvol(i) did not differ significantly between groups, diastolic filling appears largely preserved. This could suggest that the left ventricle is adapting to increased pressure overload by developing concentric hypertrophy rather than undergoing significant dilation. While this type of remodelling may help temporarily maintain cardiac function, the observed reduction in EF, despite remaining above 50%, may indicate early signs of ventricular dysfunction, potentially affecting both systolic and diastolic performance.

Even though we observed significantly higher transvalvular peak velocity and peak gradient, indicating hemodynamically significant aortic stenosis, determining the exact severity of stenosis in mice remains challenging, as standardized thresholds for severe stenosis in small animals are not well established (Casaclang-Verzosa et al., 2017). Nevertheless, previous studies have suggested a threshold for significant AS in mice to be around 1500 mm/s (Scatena et al., 2018), which aligns with our findings. Additionally, the extensive plaque formation in the aortic root may affect to transvalvular doppler flow measurements.

Overall, these results suggest that the CAVD group exhibited hemodynamically significant aortic valve narrowing and alterations in cardiac function. Further studies are needed to better understand the progression of these changes over time, how to best evaluate stenosis severity in this model, and whether the severity of stenosis is primarily due to plaque formation or CAVD progression.

## 3.2 Al$^{18}$F-NOTA-folate uptake in the aortic valve

In this study we observed clear tracer accumulation in the aortic valve of the CAVD group when using Al$^{18}$F-NOTA-folate PET, whereas similar detectable accumulation was not seen in the control group. Furthermore, data analysis revealed a statistically significant difference between the two groups ($p < 0.0001$) suggesting higher expression of FR-β in aortic valve region of the CAVD group compared to the control group.

It has been reported that FR-β expression is high in activated macrophages but not in resting ones (Lu et al., 2021). Additionally, it is known that macrophages coordinate the differentiation of VICs into aVICs and subsequently oVICs through several proinflammatory cytokines (Aikawa et al., 2007), which remodel the extracellular matrix and promote the progression of CAVD. Therefore, our results indicate a higher presence of macrophages and greater activity related to inflammation and fibro-calcific processes in the aortic valve region of the CAVD group.

The only PET tracer that has been used to evaluate the inflammation related to CAVD is $^{18}$F-FDG. A major limitation of this tracer is its high physiological uptake in the nearby myocardium, which masks the signal in the region of the aortic valve (Abdelbaky et al., 2015). In contrast, similar limitations are not observed within Al$^{18}$F-NOTA-folate due to its specificity towards FR-β expression (Jahandideh et al., 2020; Silvola et al., 2018). Our findings align with these observations, as Al$^{18}$F-NOTA-folate uptake was low in both the blood and myocardium.

In this study, $^{18}$F-NaF was used as a reference tracer because it has been shown in several studies to detect microcalcification in the aortic valves of patients with AS and has the potential to predict disease development and progression (Dweck et al., 2014; Pawade et al., 2016; Zheng et al., 2019). We observed significantly higher aortic valve $^{18}$F-NaF uptake in the CAVD group, indicating pro-calcific processes in the aortic valve region. However, the difference between the groups was less pronounced compared to the folate uptake in the same region. These findings suggest that the CAVD group is undergoing the early phase of CAVD, as microcalcification is a hallmark of this stage.

However, there are some limitations to these analyses. We did not use a contrast agent in the $^{18}$F-NaF PET imaging, making it challenging to precisely identify the aortic valve area. To address this, we merged the NaF and folate contrast-enhanced CT images for better visualization of the heart. Despite this approach, accurately defining the aortic valve remained challenging due to variations in animal positioning across imaging sessions.

The small diameter of the mouse aortic valve (approximately 1–2 mm) presents another challenges for annotation and approaches the PET imaging resolution limit (1–2 mm) (DiFilippo, 2007). Moreover, cardiac and respiratory motion during PET/CT imaging can impact the accuracy of image analysis. To enhance reliability, having two independent researchers annotate the aortic valve in PET analyses could provide more robust and reproducible results. Additionally, while we annotated the aortic valve in the sagittal plane in this study, future studies should consider annotation in the proper transaxial plane. Unfortunately, this is not possible in the version of the Carimas software we used.

Autoradiography analyses were conducted to confirm valvular Al$^{18}$F-NOTA-folate uptake. We did not observe significant difference in valve leaflets` absolute PSL/mm$^2$ values between the groups. Similarly, we did not observe significant difference in myocardium PSL/mm$^2$ values. However, significant difference was shown when leaflets PSL/mm$^2$ values were adjusted to myocardium values within higher TBR in CAVD group. In autoradiography analyses the adjustment of interested region-to-background is validated and valuable method to normalize tracer uptake in the target tissue to background region. This method takes into consideration the nonspecific binding and variability in tracer distribution, improving the accuracy and reliability of the results. However, the control group showed higher $Al^{18}F$-NOTA-folate uptake myocardium, which could lead to a lower TBR in this group.

Lastly, we observed that $Al^{18}F$-NOTA-folate uptake in the plaques of the aortic root could be a confounding factor when addressing the aim: can $Al^{18}F$-NOTA-folate PET detect FR-β expression in the aortic valves? $Al^{18}F$-NOTA-folate uptake was significantly higher in the plaques of the aortic root, approximately 2.5 times greater than in the leaflets. This indicates that a portion of the SUV signal in aortic valve PET imaging likely originates from plaque uptake, which may obscure the true SUV of the aortic valve itself. This overlap could affect both visual interpretation of the images and quantitative data analyses, making it challenging to distinguish specific valve uptake.

## 3.3 Macrophages and microcalcification related to early phase of CAVD

In histological analyses, we observed thickened aortic valves in CAVD mice compared to the control group, which was confirmed through quantitative analysis. This finding is consistent with previous studies reporting morphological changes in valve leaflets during CAVD progression (Dweck et al., 2014; Scatena et al., 2018). In Mac-3 staining analysis, we observed that the absolute area of Mac-3 staining was significantly higher in the CAVD group compared to the control group. This suggests an increase in macrophage presence in the leaflets, and potentially increased inflammation and fibro-calcific processes in the aortic valve.

However, when calculating the percentage of valve area positive for macrophages, we did not observe a statistically significant difference between the groups. This suggests that the variation in macrophage presence may not be due to a higher proportion of macrophages in the tissue but rather reflects the increased size of the aortic valve in the CAVD group. However, no validated methods currently exist for quantifying macrophage levels in the aortic valve during CAVD.

Nevertheless, we observed larger, continuous areas of Mac-3 positive staining in the CAVD group compared to the control group, indicating macrophage clusters and signs of pathological changes. In contrast, the control group cryosections did not show a similar pattern, and the Mac-

3 positive staining was inconsistent, appearing in small, scattered areas across the leaflet rather than forming a clear, organized areas.

Mac-3 has been shown to stain both activated macrophages and fibroblast-lineage cells, especially in fibrotic tissues (Inoue et al., 2005). Because CAVD involves fibrosis and activation of myofibroblast like VICs, it could be possible that some of the Mac-3 positive staining is originated from these cells rather than macrophages. Additionally, it is reported that Mac-3 is not only specific to activated macrophages, as it also stains resident macrophages involved in normal tissue homeostasis (Ho & Springer, 1983). These factors could explain why we did not observe a clearer difference between groups.

Dark black regions were detected inside the leaflets in both groups, which are most likely melanin pigment rather than macrophages (Nasim et al., 2024). These pigmented aortic valves were a confounding factor, as the Image-J software falsely detected these areas as positive for Mac-3 staining. Even after manually excluding these areas from the analysis, distinguishing true positive staining from false positives remained challenging in some cases, potentially affecting the results.

Alizarin Red S is known to detect late-stage calcification in the extracellular matrix (Qureshi et al., 2014). In this analysis, we identified small, individual calcium deposits inside the leaflets, primarily located at their insertions. Additionally, heavy calcium accumulation was observed in plaque formations around the aortic root. In contrast, no calcium deposits were detected in the control group. A crucial aspect of this study was selecting the appropriate endpoint to detect the early phase of CAVD rather than its late stage. Based on these results, the chosen endpoint appears appropriate, as the pathological progression of the disease was observed without reaching the end stage and supported with $^{18}$F-NaF PET analyses.

However, supportive studies are needed and additional endpoints, such as at 6 and 9 months of age, could provide more information on disease progression and the feasibility of using Al$^{18}$F-NOTA-folate. Moreover, CAVD have shown to have a sex-specific phenotype, where females are more prone to develop a fibrotic disease phenotype, while males show a higher susceptibility to calcium deposits (Lindman & Merryman, 2021). Therefore, it would be interesting to investigate whether a similar phenotype is observed in mice.

For future studies, more specific immunohistochemical assays targeting activated macrophages could offer deeper insights into their role in CAVD. Using macrophage-type-specific antibodies, such as anti-iNOS for pro-inflammatory macrophages and anti-CD206 for anti-inflammatory macrophages, could be particularly informative. Additionally, FR-β antibodies in these immunoassays could provide valuable information about FR-β co-localization with specific macrophage subtypes. If combined with additional time points, these assays could help detect shifts between pro-inflammatory and anti-inflammatory macrophages and determine whether such changes affect Al$^{18}$F-NOTA-folate uptake in the valve leaflets. Furthermore, future studies will include immunostainings related to fibrosis.

## 3.4 Evaluating association between the echocardiography and Al$^{18}$F-NOTA-folate uptake with histological findings

In the correlation analysis, we observe a strong correlation between Mac-3-positive areas and peak transvalvular velocity comparisons. Moreover, a moderate correlation was observed between aortic valve $SUV_{mean}$ on PET and peak transvalvular velocity, whereas correlation between aortic valve $SUV_{mean}$ and immunohistochemical comparisons were not observed.

A strong positive correlation with a significant p-value in the immunoassay-to-peak velocity comparison indicates a relationship between activated macrophage levels and the severity of stenosis, where higher macrophage levels and increased inflammatory activity are associated with more severe AS. Moreover, this phenomenon appears to be disease-specific, as a similar correlation was not observed in the control group. Additionally, morphological changes in the valve leaflets of CAVD mice were observed, aligning with these correlation results.

A moderate correlation between the aortic valve $SUV_{mean}$ on PET and the echocardiographic peak transvalvular velocity in the CAVD group indicates a modest relationship between the severity of AS and folate uptake, with a disease-specific correlation, as no association was observed in the control group. The most probable reason for the lack of correlation between the aortic valve $SUV_{mean}$ on PET and activated macrophage levels in the valve leaflets is the excessive plaque formation and its spillover effect in the aortic root, which may mask the precise $SUV_{mean}$ of the valve leaflets.

Drawing deeper conclusions from these correlation analyses is challenging due to the small sample size and conflicting results. Moreover, we must interpret these findings from a clinical perspective also, rather than focusing only on individual numerical values. For instance, some echocardiography results indicate significant aortic stenosis affecting cardiac performance. In contrast, the valve leaflets` modestly higher folate uptake, seen in the autoradiography analyses and the presence of small individual calcium deposits in Alizarin Red S analyses suggest the early phase of the disease. The difference between the advanced findings in echocardiography and the early-stage indicators in autoradiography and immunostainings may partly explain the weak statistical correlation analyses.

### 3.5 Considerations on mouse models

As we know, no animal model perfectly mimics human diseases. However, previous studies (Sider et al., 2011) suggest that the LDLR $^{-/-}$ ApoB100/100 mouse is one the most promising model for studying CAVD. LDLR$^{-/-}$ ApoB100/100 mice have shown to develop hemodynamically significant AS, thickened aortic valve leaflets, and calcification when placed on a modified diet. This model also exhibits reduced EF and fractional shortening, indicating impaired cardiac function (Scatena et al., 2018) In this study we observed similar findings: transaortic peak velocity and peak gradient was significantly higher, the area of leaflets was larger, small calcification deposits were detected and reduced EF and cardiac performance was observed in CAVD group.

However, this animal model is not specifically designed to mimic CAVD but rather atherosclerotic diseases. Although high plasma lipid and triglyceride levels are risk factors for CAVD, they are not the only independent factors contributing to the disease. While CAVD and atherosclerosis share some common risk factors and pathological processes, extensive plaque formation under the endothelium of the aorta near the aortic root is not a typical finding in human CAVD (Olsson et al., 1999).

The structure of the mouse aortic valve differs from humans. While the human aortic valve has a tri-layered architecture, comprising the fibrosa, spongiosa, and ventricularis layers, mice lack this distinct organization and have a valve that is approximately 5-10 cells thick (Sider et al., 2011). This structural difference is important to note, as it may influence pathological processes in the aortic valve, including susceptibility to calcification and therefore its translational potential.

In biodistribution analyses, we observed that the control group had higher folate uptake in the myocardium, in small intestine and in lungs compared to the CAVD group. Additionally, we noted that the mean weight of the control group was significantly higher, and visceral fat accumulation was observed in the chest and abdominal cavity during tissue collection. These findings suggest that the control group may have some degree of systemic inflammation associated with obesity. However, to confirm systemic inflammation, additional studies, such as cytokine profiling, are needed.

These findings highlight some important points what should be considered in the future studies. The control group was set to represent age-matched healthy individuals. However, based on these observations, it seems that they may not fully reflect this characterization. The potential presence of systemic inflammation and lipid infiltration in myocardium could influence to the results. Since aging is an independent risk factor strongly correlated with the incidence of CAVD, it would be reasonable to use younger mice as a control group. Although spontaneous CAVD is not observed in mice, early signs of CAVD-related processes, such as increased macrophage levels or age-related fibrotic changes, could affect leaflet integrity and flexibility.

## 3.6 Translational aspects

In this study, we have taken an important first step toward enabling the detection of early-phase CAVD by successfully visualizing and quantifying inflammation in the aortic valve region, despite the extremely small target size. Detecting such inflammation in larger subjects, such as humans, would likely be more straightforward. The ability to identify early-stage CAVD would be a crucial tool for evaluating both novel and existing drug candidates. One possible reason for drug failures in CAVD treatment could be that interventions are applied too late when the disease has already progressed to an irreversible stage.

Furthermore, the sex-specific phenotype of CAVD presents an additional challenge for drug discovery and disease management. The ability to assess early-phase inflammation could enhance precision medicine approaches and help address this hurdle.

If FR-β expression is elevated in human aortic valve leaflets during the early phase of the disease, it could serve as a promising drug target for attenuating inflammation by specifically targeting activated inflammatory cells. This strategy could provide a more targeted approach compared to methotrexate, which modulates folate metabolism but lacks specificity toward activated inflammatory cells, potentially leading to systemic side effects. These side effects can be particularly problematic in the management of inflammation-driven diseases. By selectively targeting activated inflammatory cells, this approach may reduce adverse effects, improve treatment adherence, and enhance therapeutic precision.

Moreover, there is growing interest in developing imaging-guided therapy, where the molecular imaging target and therapeutic target are the same, allowing for patient selection, optimized treatment timing, and disease monitoring through PET imaging.

However, when considering the broader challenges of CAVD, it is important to recognize that even with effective imaging techniques for early detection and medications to slow disease progression, screening patients at an early stage will remain difficult due to the asymptomatic nature of CAVD. Addressing this challenge should be a key focus of future research.

## 3.7 Conclusions

These results suggest that Al$^{18}$F-NOTA-folate PET can detect inflammation in the aortic valve region of an experimental CAVD mouse model and may be a promising tool for assessing early-phase disease. However, further detailed investigation is needed to determine the precise origin of the signal observed in PET/CT imaging.

# 4 Materials and methods

## 4.1 Design of the study

One-year-old atherosclerotic low-density lipoprotein receptor deficient mice expressing only apolipoprotein B100 (LDLR$^{-/-}$ApoB$^{100/100}$, strain #003000, The Jackson Laboratory, Bar Harbor, ME, USA) were fed with a high-fat diet (0.2% total cholesterol, TD 88137 mod., ssniff Spezialdiäten Gmbh, Soest, DE) for 8 months to induce experimental CAVD. Healthy age-matched C57BL/6N mice, fed with a regular chow diet, served as controls. Eight mice, four females and four males were included in both groups, having 16 mice in total in this study.

Firstly, echocardiography was performed to assess the development of AS. Main measures included peak aortic valve velocity, peak transvalvular gradient, and ejection fraction. Thereafter, mice underwent imaging with both $^{18}$F-NaF and Al$^{18}$F-NOTA-folate PET/CT, having at least three-day recovery between imaging. Following Al$^{18}$F-NOTA-folate PET/CT imaging, blood samples were obtained via cardiac puncture. The mice were then euthanized through cervical dislocation under deep anaesthesia, and tissues were collected for gamma counting to assess ex vivo biodistribution. Detailed analysis of Al$^{18}$F-NOTA-folate uptake in the aortic valves was performed using autoradiography on tissue sections, alongside immunohistological validation of the same sections. Stainings included inflammatory and calcific markers. (Figure 2).

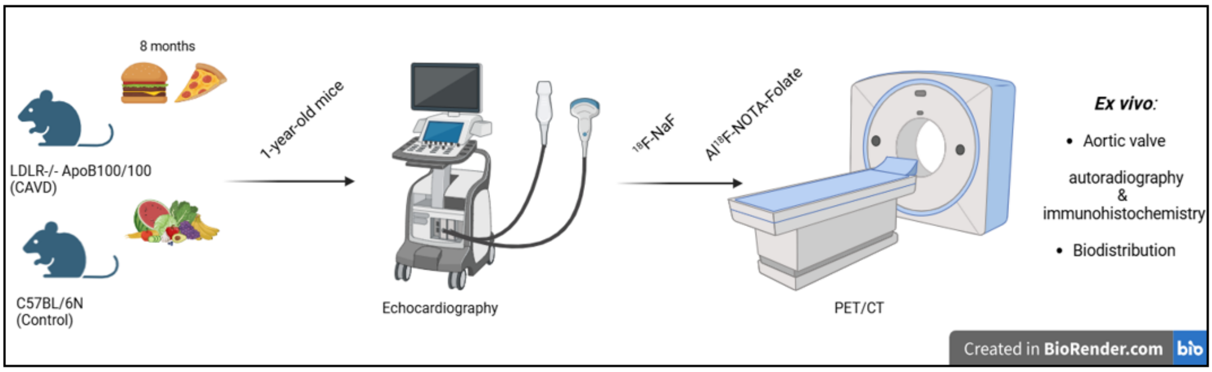

**Figure X. Study Design.** One-year-old atherosclerotic LDLR$^{-/-}$ApoB$^{100/100}$ mice, fed a high-fat diet for 8 months, were used as an experimental model of CAVD, while age-matched C57BL/6N mice on a regular chow diet served as controls. Echocardiography was performed to assess cardiac function, followed by PET/CT imaging using $^{18}$F-NaF and $^{18}$F-NOTA-folate tracers, with $^{18}$F-NaF serving as a reference tracer. After imaging, ex vivo autoradiography and histological analysis of aortic valve samples were conducted for validation.

Animal experiments are approved by the national Animal Experiment Board in Finland and the Regional State Administrative Agency for Southern Finland (License number 14700/2024). Studies are conducted in compliance with the European Union legislation. The animals were housed under standard conditions at the Central Animal Laboratory, University of Turku, with a 12-hour light cycle (lights on from 6:00 a.m. to 6:00 p.m.) and had free access to food and water throughout the study.

## 4.2 Echocardiography

Transthoracic echocardiography was performed to evaluate aortic valve hemodynamics, and cardiac function was assessed using a specialized small animal ultrasound system (Vevo 2100, Visual Sonics Inc., Toronto, Canada) equipped with a linear 22–55 MHz transducer (MS550D). Mice were anesthetized with isoflurane (4% for induction and 1–2% for maintenance; Attane Vet 1000 mg/g, Primal Healthcare UK Limited, UK), and body temperature was maintained using a heating pad.

Transvalvular blood flow in the aorta was identified using colour Doppler mapping in modified parasternal long-axis views, and the flow velocity profile was captured with pulsed-wave Doppler imaging. Angle correction of 40-45° was implemented and peak aortic valve flow velocity (mm/s) and peak transvalvular gradient (mmHg) were measured. Parasternal B-mode long-axis (2D) images were acquired to measure LV ejection fraction and LV diastolic and systolic volumes indexed to body weight (LVDvol(i), LVSvol(i), respectively). Image analysis was conducted using the VevoLab software (version 5.5.0).

The LVDvol(i) and LVSvol(i) were calculated using the following equations:

$$LVDvol(i) = LV\ diastolic\ volume\ /\ Body\ weight$$

$$LVSvol(i) = LV\ systolic\ volume\ /\ Body\ weight$$

where LVDvol(i) and LVSvol(i) are expressed in µL/g.

## 4.3 Radiochemistry

PET tracers were produced at the Radiopharmaceutical Chemistry Laboratory of the Turku PET Centre. The synthesis of $^{18}$F-NaF followed a standard clinical protocol, while Al$^{18}$F-NOTA-folate was prepared according to a previously published method (Silvola et al., 2018). For both tracers, the radiochemical purity consistently exceeded 95% in all batches.

## 4.4 *In vivo* PET/CT imaging and biodistribution

For PET/CT imaging, mice were anesthetized with isoflurane (3-4% for induction and 1-2% for maintenance) and body temperature was maintained with a heating pad. A tail vein catheter was put in place and the following radioactivity doses were injected: 4.3 ± 0.06 MBq of $^{18}$F-NaF and 9.9 ± 0.12 MBq of Al$^{18}$F-NOTA-folate. The mice were imaged using a dedicated small-animal PET/CT scanners, Molecubes X-CUBE and β-CUBE (Molecubes, Gent, Belgium). $^{18}$F-NaF PET imaging was conducted as a static 20-minute PET acquisition 40 minutes after injection, while Al$^{18}$F-NOTA-folate PET imaging was conducted as a 60-minute dynamic acquisition (six 10-s, four 60-s, five 300-s, and three 600-s time frames). After Al$^{18}$F-NOTA-folate PET imaging, an iodinated contrast agent (100 µL of eXIATM160XL, Binitio Biomedical Inc., Ottawa, ON, Canada) was injected for high-resolution contrast-enhanced CT to visualize aorta and endocardial border.

Carimas 2.9 software (Turku PET Centre, Turku, Finland) was used to analyse the PET/CT images. PET and CT images were automatically superimposed, the ROIs were defined in the aortic valve, blood (LV cavity), aortic arch (plaques), myocardium, liver, lungs, sternum, spleen, kidney, and urinary bladder. In $^{18}$F-NaF PET, myocardium ROI were defined in interventricular septum, whereas in folate PET in anterolateral wall. The ROIs uniform sizes were verified using data from Carimas software. Results were expressed as mean standardized uptake values (SUV$_{\text{mean}}$) in time frames 50-60 post-injection, which means normalization for injected radioactivity dose and animal body weight. Mean target-to-background ratios (TBR) were calculated as:

$$SUV\ mean, aortic\ valve\ /\ SUV\ mean, blood\ pool$$

The ex vivo biodistribution of Al$^{18}$F-NOTA-folate tracer was analysed immediately following PET/CT imaging. Mice were euthanized using cardiac puncture and cervical dislocation methods. Glucose values were measured from the terminal blood samples using a glucometer (Bayer Contour, Bayer AG, Leverkusen, Germany). Tissues were excised and the uptake of the tracer in various organs was measured using a Wizard Automatic 2480 gamma counter

(PerkinElmer). Results were expressed as SUVs, which were normalized for the injected radioactive dose, animal body weight, and tissue weight.

## 4.5 *Ex vivo* autoradiography, histology, and immunostaining

To enable detailed quantification of Al$^{18}$F-NOTA-folate uptake in the aortic valves, the heart was washed with saline to eliminate residual blood, then excised, frozen in precooled isopentane, and sectioned transversely at the level of the aortic root into sequential cryosections of 20 and 8 μm thickness. The sections were placed on imaging plates (Fuji Imaging Plate BAS-TR2025, Fuji Photo Film Co., Ltd., Tokyo, Japan) and exposed for 3.5 to 5 hours. Subsequently, the plates were scanned using the Fuji Analyzer BAS-5000 (Fuji, Tokyo, Japan) with an internal resolution of 25 μm.

The 20-μm sections were stained with haematoxylin and eosin (H&E). Autoradiographs were co-registered with H&E images, and the uptake of Al$^{18}$F-NOTA-folate was measured using the following ROIs: valve leaflets, plaques of the aorta, and myocardium nearby of the aortic root. The results were expressed as mean photo-stimulated luminescence per square millimetre (PSL/mm$^2$) using Carimas 2.9 software (Turku PET Centre, Turku, Finland). Background radiation was subtracted from the actual ROIs, and the results were normalized for decay portion of the tracer and exposure time**.** Average Al$^{18}$F-NOTA-folate uptake within valves was divided by the average uptake in myocardium (expressed as valve-to-myocardium ratio) in each mouse.

For immunohistochemistry, adjacent 8-μm cryosections were stained with Mac-3 (CD107b/LAMP-2, #550292, BD Pharmingen) to evaluate the presence of macrophages and Alizarin Red S (#TMS-008-C, Sigma-Aldrich) to detect calcium deposits. Sections were scanned with Pannoramic 1000 digital scanner (Hungary, 3DHISTECH) Mac-3 immunohistochemistry staining was analysed using ImageJ software (Fiji-win32) with commercially available analysis tools. Aortic leaflets were annotated from five different sections in both groups. The following parameters were assessed: the mean total valve area, the mean total Mac-3-stained area, and the percentage of Mac-3-stained area, calculated using the following equation:

$$Mean\ of total\ valve\ area\ /\ Mean\ of\ total\ Mac-3-stained\ area\ X\ 100\%$$

Histological findings were correlated with echocardiography and PET results.

## 4.6 Statistical methods

All results are reported as mean ± standard deviation (SD). Comparisons of unpaired data between two groups were conducted using the Student`s t-test or Welch's t-test, depending on variance equality. Levene's test was used to assess variance equality between groups. Correlations between two continuous variables were analysed using Pearson's correlation test. The Shapiro-Wilk test was used to assess normality. All graphs and statistical analyses were performed using GraphPad Prism, version 10 (GraphPad Software Inc., La Jolla, CA, USA). A p-value < 0.05 was considered statistically significant.

# 5 Acknowledgements

I would like to thank PhD Mia Ståhle and Professor Anne Roivainen for their guidance and support throughout this project. I also appreciate the contributions of all the members at the Turku PET Centre and Histocore, whose efforts made this project possible.

# 6 Abbreviations

AS: Aortic stenosis

AVR: Arterial valve replacement

B-mode: (two-dimensional brightness mode)

CAVD: Calcific aortic valve disease

CCT: non-contrast cardiac computed tomography

DAMPs: Danger-Associated Molecular Patterns

ECM: Extracellular matrix

EF: Ejection fraction

EndMT: Endothelial-to-mesenchymal transition

FR-α: Folate receptor alpha

FR-β: Folate receptor beta.

FS: Fractional shortening

IL: Interleukin

LDL: Low density lipoprotein

Lp (a): Lipoprotein(a)

LV: Left ventricular

LVDvol(i): Left ventricular diastolic volume indexed

LVH: Left ventricular hypertrophy

LVSvol(i): Left ventricular systolic volume indexed

M1: Pro-inflammatory macrophages

M2: Anti-inflammatory macrophages

M-CSF: Maturation mediator macrophage colony stimulating factor

M-mode: Motion mode

oxLDL: Oxidized LDL cholesterol

PET: Positron emission tomography

RAAS: Renin-Angiotensin-Aldosterone-System

VEC: Valvular endothelial cell

VIC: Valve interstitial cell

aVIC: Activated myofibroblast-like VIC

eVIC: Endothelial-derived VIC

oVIC: Osteoblastic VIC

qVIC: Quiescent VIC

NaF: Sodium fluoride

$^{18}$F-FOL: Aluminium $^{18}$F-labeled 1,4,7-triazacyclononane-N, N′, N″-triacetic acid conjugated folate

$^{18}$F-NaF: Fuorine-18-labelled NaF

$^{18}$F-FDG: 2-deoxy-2-[18F] fluoro-D-glucose

## References

Abdelbaky, A., Corsini, E., Figueroa, A. L., Subramanian, S., Fontanez, S., Emami, H., Hoffmann, U., Narula, J., & Tawakol, A. (2015). Early aortic valve inflammation precedes calcification: A longitudinal FDG-PET/CT study. *Atherosclerosis*, *238*(2), 165–172. https://doi.org/10.1016/j.atherosclerosis.2014.11.026

Ahuja, K., Sotoudeh, H., Galgano, S. J., Singh, R., Gupta, N., Gaddamanugu, S., & Choudhary, G. (2020). 18F-Sodium Fluoride PET: History, Technical Feasibility, Mechanism of Action, Normal Biodistribution, and Diagnostic Performance in Bone Metastasis Detection Compared with Other Imaging Modalities. *Journal of Nuclear Medicine Technology*, *48*(1), 9–16. https://doi.org/10.2967/jnmt.119.234336

Aikawa, E., Nahrendorf, M., Figueiredo, J.-L., Swirski, F. K., Shtatland, T., Kohler, R. H., Jaffer, F. A., Aikawa, M., & Weissleder, R. (2007). Osteogenesis associates with inflammation in early-stage atherosclerosis evaluated by molecular imaging in vivo. *Circulation*, *116*(24), 2841–2850. Scopus. https://doi.org/10.1161/CIRCULATIONAHA.107.732867

Bartoli-Leonard, F., Zimmer, J., & Aikawa, E. (2021). Innate and adaptive immunity: The understudied driving force of heart valve disease. *Cardiovascular Research*, *117*(13), 2506–2524. https://doi.org/10.1093/cvr/cvab273

Blankstein, R., Osborne, M., Naya, M., Waller, A., Kim, C. K., Murthy, V. L., Kazemian, P., Kwong, R. Y., Tokuda, M., Skali, H., Padera, R., Hainer, J., Stevenson, W. G., Dorbala, S., & Di, C. M. F. (2014). Cardiac Positron Emission Tomography Enhances Prognostic Assessments of Patients With Suspected Cardiac Sarcoidosis. *Journal of the American College of Cardiology*, *63*(4), 329–336. https://doi.org/10.1016/j.jacc.2013.09.022

Bornstein, A. B., Rao, S. S., & Marwaha, K. (2023). Left Ventricular Hypertrophy. In *StatPearls [Internet]*. StatPearls Publishing. https://www.ncbi.nlm.nih.gov/books/NBK557534/

Boyd, D. P. (2007). Instrumentation and Principles of CT. In M. F. Di Carli & M. J. Lipton (Eds.), *Cardiac PET and PET/CT Imaging* (pp. 19–33). Springer. https://doi.org/10.1007/978-0-387-38295-1_2

Braga, T. T., Agudelo, J. S. H., & Camara, N. O. S. (2015). Macrophages During the Fibrotic Process: M2 as Friend and Foe. *Frontiers in Immunology*, *6*, 602. https://doi.org/10.3389/fimmu.2015.00602

Butcher, J. T., & Nerem, R. M. (2006). Valvular Endothelial Cells Regulate the Phenotype of Interstitial Cells in Co-culture: Effects of Steady Shear Stress. *Tissue Engineering*, *12*(4), 905–915. https://doi.org/10.1089/ten.2006.12.905

Capelleveen, J. C. van, Valk, F. M. van der, & Stroes, E. G. (2016). Current therapies for lowering lipoprotein (a). *Journal of Lipid Research*, *57*(9), 1612–1618. https://doi.org/10.1194/jlr.R053066

Capoulade, R., Yeang, C., Chan, K. L., Pibarot, P., & Tsimikas, S. (2018). Association of Mild to Moderate Aortic Valve Stenosis Progression With Higher Lipoprotein(a) and Oxidized Phospholipid Levels: Secondary Analysis of a Randomized Clinical Trial. *JAMA Cardiology*, *3*(12), 1212–1217. https://doi.org/10.1001/jamacardio.2018.3798

Casaclang-Verzosa, G., Enriquez-Sarano, M., Villaraga, H. R., & Miller, J. D. (2017). Echocardiographic Approaches and Protocols for Comprehensive Phenotypic Characterization of Valvular Heart Disease in Mice. *Journal of Visualized Experiments : JoVE*, *120*, 54110. https://doi.org/10.3791/54110

Chalajour, F., Treede, H., Gehling, U. M., Ebrahimnejad, A., Boehm, D. H., Riemer, R. K., Ergun, S., & Reichenspurner, H. (2007). Identification and characterization of cells with high angiogenic potential and transitional phenotype in calcific aortic valve. *Experimental Cell Research*, *313*(11), 2326–2335. https://doi.org/10.1016/j.yexcr.2007.02.033

Chan, K. L., Teo, K., Dumesnil, J. G., Ni, A., & Tam, J. (2010). Effect of Lipid Lowering With Rosuvastatin on Progression of Aortic Stenosis. *Circulation*, *121*(2), 306–314. https://doi.org/10.1161/CIRCULATIONAHA.109.900027

Coffey, S., Cox, B., & Williams, M. J. A. (2014). The Prevalence, Incidence, Progression, and Risks of Aortic Valve Sclerosis: A Systematic Review and Meta-Analysis. *Journal of the American College of Cardiology*, *63*(25, Part A), 2852–2861. https://doi.org/10.1016/j.jacc.2014.04.018

Cowell, S. J., Newby, D. E., Prescott, R. J., Bloomfield, P., Reid, J., Northridge, D. B., & Boon, N. A. (2005). A randomized trial of intensive lipid-lowering therapy in calcific aortic stenosis. *New England Journal of Medicine*, *352*(23), 2389–2397. Scopus. https://doi.org/10.1056/NEJMoa043876

Crawford, P. T., Arbor, T. C., & Bordoni, B. (2023). Anatomy, Thorax, Aortic Valve. In *StatPearls [Internet]*. StatPearls Publishing. https://www.ncbi.nlm.nih.gov/books/NBK559384/

d’Arcy, J. L., Coffey, S., Loudon, M. A., Kennedy, A., Pearson-Stuttard, J., Birks, J., Frangou, E., Farmer, A. J., Mant, D., Wilson, J., Myerson, S. G., & Prendergast, B. D. (2016). Large-scale community echocardiographic screening reveals a major burden of undiagnosed valvular heart disease in older people: The OxVALVE Population Cohort Study†. *European Heart Journal*, *37*(47), 3515–3522. https://doi.org/10.1093/eurheartj/ehw229

DiFilippo, F. P. (2007). Instrumentation and Principles of Imaging: PET. In M. F. Di Carli & M. J. Lipton (Eds.), *Cardiac PET and PET/CT Imaging* (pp. 3–18). Springer. https://doi.org/10.1007/978-0-387-38295-1_1

Dweck, M. R., Aikawa, E., Newby, D. E., Tarkin, J. M., Rudd, J. H. F., Narula, J., & Fayad, Z. A. (2016). Noninvasive Molecular Imaging of Disease Activity in Atherosclerosis. *Circulation Research*, *119*(2), 330–340. https://doi.org/10.1161/CIRCRESAHA.116.307971

Dweck, M. R., Jenkins, W. S. A., Vesey, A. T., Pringle, M. A. H., Chin, C. W. L., Malley, T. S., Cowie, W. J. A., Tsampasian, V., Richardson, H., Fletcher, A., Wallace, W. A., Pessotto, R., van Beek, E. J. R., Boon, N. A., Rudd, J. H. F., & Newby, D. E. (2014). 18F-Sodium Fluoride Uptake Is a Marker of Active Calcification and Disease Progression in Patients With Aortic Stenosis. *Circulation: Cardiovascular Imaging*, *7*(2), 371–378. https://doi.org/10.1161/CIRCIMAGING.113.001508

El Accaoui, R. N., Gould, S. T., Hajj, G. P., Chu, Y., Davis, M. K., Kraft, D. C., Lund, D. D., Brooks, R. M., Doshi, H., Zimmerman, K. A., Kutschke, W., Anseth, K. S., Heistad, D. D., & Weiss, R. M. (2014). Aortic valve sclerosis in mice deficient in endothelial nitric oxide synthase. *American Journal of Physiology - Heart and Circulatory Physiology*, *306*(9), H1302–H1313. Scopus. https://doi.org/10.1152/ajpheart.00392.2013

Garg, R., & Yusuf, S. (1995). Overview of randomized trials of angiotensin-converting enzyme inhibitors on mortality and morbidity in patients with heart failure. Collaborative Group on ACE Inhibitor Trials. *JAMA*, *273*(18), 1450–1456.

Gonzales, H., Douglas, P. S., Pibarot, P., Hahn, R. T., Khalique, O. K., Jaber, W. A., Cremer, P., Weissman, N. J., Asch, F. M., Zhang, Y., Gertz, Z. M., Elmariah, S., Clavel, M.-A., Thourani, V. H., Daubert, M., Alu, M. C., Leon, M. B., & Lindman, B. R. (2020). Left Ventricular Hypertrophy and Clinical Outcomes Over 5 Years After TAVR. *JACC: Cardiovascular Interventions*, *13*(11), 1329–1339. https://doi.org/10.1016/j.jcin.2020.03.011

Grego-Bessa, J., Pérez-Pomares, J. M., & Luis de la Pompa, J. (2010). Chapter 6.2 - Signaling Pathways in Valve Formation: The Origin of Congenital Defects. In N. Rosenthal & R. P. Harvey (Eds.), *Heart Development and Regeneration* (pp. 389–413). Academic Press. https://doi.org/10.1016/B978-0-12-381332-9.00019-0

Helas, S., Goettsch, C., Schoppet, M., Zeitz, U., Hempel, U., Morawietz, H., Kostenuik, P. J., Erben, R. G., & Hofbauer, L. C. (2009). Inhibition of receptor activator of NF-kappaB ligand by denosumab attenuates vascular calcium deposition in mice. *The American Journal of Pathology*, *175*(2), 473–478. https://doi.org/10.2353/ajpath.2009.080957

Hjortnaes, J., Shapero, K., Goettsch, C., Hutcheson, J. D., Keegan, J., Kluin, J., Mayer, J. E., Bischoff, J., & Aikawa, E. (2015). Valvular interstitial cells suppress calcification of valvular endothelial cells. *Atherosclerosis*, *242*(1), 251–260. https://doi.org/10.1016/j.atherosclerosis.2015.07.008

Ho, M. K., & Springer, T. A. (1983). Tissue distribution, structural characterization, and biosynthesis of Mac-3, a macrophage surface glycoprotein exhibiting molecular weight heterogeneity. *The Journal of Biological Chemistry*, *258*(1), 636–642.

Hulin, A., Hortells, L., Gomez-Stallons, M. V., O'Donnell, A., Chetal, K., Adam, M., Lancellotti, P., Oury, C., Potter, S. S., Salomonis, N., & Yutzey, K. E. (2019). Maturation of heart valve cell populations during postnatal remodeling. *Development (Cambridge, England)*, *146*(12), dev173047. https://doi.org/10.1242/dev.173047

Hyder, J. A., Allison, M. A., Wong, N., Papa, A., Lang, T. F., Sirlin, C., Gapstur, S. M., Ouyang, P., Carr, J. J., & Criqui, M. H. (2009). Association of coronary artery and aortic calcium with lumbar bone density: The MESA Abdominal Aortic Calcium Study. *American Journal of Epidemiology*, *169*(2), 186–194. https://doi.org/10.1093/aje/kwn303

Ingersoll, M. A., Spanbroek, R., Lottaz, C., Gautier, E. L., Frankenberger, M., Hoffmann, R., Lang, R., Haniffa, M., Collin, M., Tacke, F., Habenicht, A. J. R., Ziegler-Heitbrock, L., & Randolph, G. J. (2010). Comparison of gene expression profiles between human and mouse monocyte subsets. *Blood*, *115*(3), e10-19. https://doi.org/10.1182/blood-2009-07-235028

Inoue, T., Plieth, D., Venkov, C. D., Xu, C., & Neilson, E. G. (2005). Antibodies against macrophages that overlap in specificity with fibroblasts. *Kidney International*, *67*(6), 2488–2493. https://doi.org/10.1111/j.1523-1755.2005.00358.x

Jahandideh, A., Uotila, S., Ståhle, M., Virta, J., Li, X.-G., Kytö, V., Marjamäki, P., Liljenbäck, H., Taimen, P., Oikonen, V., Lehtonen, J., Mäyränpää, M. I., Chen, Q., Low, P. S., Knuuti, J., Roivainen, A., & Saraste, A. (2020). Folate Receptor β–Targeted PET Imaging of Macrophages in Autoimmune Myocarditis. *Journal of Nuclear Medicine*, *61*(11), 1643–1649. https://doi.org/10.2967/jnumed.119.241356

Jain, H., Goyal, A., Khan, A. T. M. A., Khan, N. U., Jain, J., Chopra, S., Sulaiman, S. A., Reddy, M. M., Patel, K., Khullar, K., Daoud, M., & Sohail, A. H. (2024). Insights into calcific aortic valve stenosis: A comprehensive overview of the disease and advancing treatment strategies. *Annals of Medicine and Surgery*, *86*(6), 3577–3590. https://doi.org/10.1097/MS9.0000000000002106

Jenkins, W. S. A., Vesey, A. T., Shah, A. S. V., Pawade, T. A., Chin, C. W. L., White, A. C., Fletcher, A., Cartlidge, T. R. G., Mitchell, A. J., Pringle, M. A. H., Brown, O. S., Pessotto, R., McKillop, G., Van Beek, E. J. R., Boon, N. A., Rudd, J. H. F., Newby, D. E., & Dweck, M. R. (2015). Valvular 18F-Fluoride and 18F-Fluorodeoxyglucose Uptake Predict Disease Progression and Clinical Outcome in Patients With Aortic Stenosis. *Journal of the American College of Cardiology*, *66*(10), 1200–1201. https://doi.org/10.1016/j.jacc.2015.06.1325

Kim, A. J., Xu, N., & Yutzey, K. E. (2020). Macrophage lineages in heart valve development and disease. *Cardiovascular Research*, *117*(3), 663–673. https://doi.org/10.1093/cvr/cvaa062

Kronenberg, F., Mora, S., Stroes, E. S. G., Ference, B. A., Arsenault, B. J., Berglund, L., Dweck, M. R., Koschinsky, M., Lambert, G., Mach, F., McNeal, C. J., Moriarty, P. M., Natarajan, P., Nordestgaard, B. G., Parhofer, K. G., Virani, S. S., Von Eckardstein, A., Watts, G. F., Stock, J. K., … Catapano, A. L. (2022). Lipoprotein(a) in atherosclerotic cardiovascular disease and aortic stenosis: A European Atherosclerosis Society consensus statement. *European Heart Journal*, *43*(39), 3925–3946. https://doi.org/10.1093/eurheartj/ehac361

Lech, M., & Anders, H.-J. (2013). Macrophages and fibrosis: How resident and infiltrating mononuclear phagocytes orchestrate all phases of tissue injury and repair. *Biochimica Et Biophysica Acta*, *1832*(7), 989–997. https://doi.org/10.1016/j.bbadis.2012.12.001

Leech, G. J., McCulloch, M. L., & Adams, D. (2018). Physical Principles of Ultrasound. In P. Nihoyannopoulos & J. Kisslo (Eds.), *Echocardiography* (pp. 3–31). Springer International Publishing. https://doi.org/10.1007/978-3-319-71617-6_1

Lindman, B. R., & Lindenfeld, J. (2021). Prevention and Mitigation of Heart Failure in the Treatment of Calcific Aortic Stenosis: A Unifying Therapeutic Principle. *JAMA Cardiology*, *6*(9), 993–994. https://doi.org/10.1001/jamacardio.2021.2082

Lindman, B. R., & Merryman, W. D. (2021). Unloading the Stenotic Path to Identifying Medical Therapy for Calcific Aortic Valve Disease: Barriers and Opportunities (Perspective). *Circulation*, *143*(15), 1455–1457. https://doi.org/10.1161/CIRCULATIONAHA.120.052531

Lindman, B. R., Sukul, D., Dweck, M. R., Madhavan, M. V., Arsenault, B. J., Coylewright, M., Merryman, W. D., Newby, D. E., Lewis, J., Harrell, F. E., Mack, M. J., Leon, M. B., Otto, C. M., & Pibarot, P. (2021). Evaluating Medical Therapy for Calcific Aortic Stenosis: JACC State-of-the-Art Review. *Journal of the American College of Cardiology*, *78*(23), 2354–2376. https://doi.org/10.1016/j.jacc.2021.09.1367

Liu, A. C., Joag, V. R., & Gotlieb, A. I. (2007). The Emerging Role of Valve Interstitial Cell Phenotypes in Regulating Heart Valve Pathobiology. *The American Journal of Pathology*, *171*(5), 1407–1418. https://doi.org/10.2353/ajpath.2007.070251

Long, H., Lichtnekert, J., Andrassy, J., Schraml, B. U., Romagnani, P., & Anders, H.-J. (2023). Macrophages and fibrosis: How resident and infiltrating mononuclear phagocytes account for organ injury, regeneration or atrophy. *Frontiers in Immunology*, *14*. https://doi.org/10.3389/fimmu.2023.1194988

Lu, Y. J., Leroy W. Wheeler, I. I., Chu, H., Kleindl, P. J., Pugh, M., You, F., Rao, S., Garcia, G., Wu, H. Y., Cunha, A. P. da, Johnson, R., Westrick, E., Cross, V., Lloyd, A., Dircksen, C., Klein, P. J., Vlahov, I. R., Low, P. S., & Leamon, C. P. (2021). Targeting folate receptor beta on monocytes/macrophages renders rapid inflammation resolution independent of root causes. *Cell Reports Medicine*, *2*(10). https://doi.org/10.1016/j.xcrm.2021.100422

Marquis-Gravel, G., Redfors, B., Leon, M. B., & Généreux, P. (2016). Medical Treatment of Aortic Stenosis. *Circulation*, *134*(22), 1766–1784. https://doi.org/10.1161/CIRCULATIONAHA.116.023997

Matherly, L. H., & Goldman, I. D. (2003). Membrane Transport of Folates. *Vitamins and Hormones*, *66*, 403–456. Scopus. https://doi.org/10.1016/S0083-6729(03)01012-4

Moncla, L.-H. M., Briend, M., Bossé, Y., & Mathieu, P. (2023). Calcific aortic valve disease: Mechanisms, prevention and treatment. *Nature Reviews Cardiology*, *20*(8), 546–559. https://doi.org/10.1038/s41569-023-00845-7

Nadra, I., Mason, J. C., Philippidis, P., Florey, O., Smythe, C. D. W., McCarthy, G. M., Landis, R. C., & Haskard, D. O. (2005). Proinflammatory Activation of Macrophages by Basic Calcium Phosphate Crystals via Protein Kinase C and MAP Kinase Pathways. *Circulation Research*, *96*(12), 1248–1256. https://doi.org/10.1161/01.RES.0000171451.88616.c2

Nasim, S., Abujamra, B. A., Chaparro, D., Nogueira, P. D. S., Riva, A., Hutcheson, J. D., & Kos, L. (2024). Multiple cell types including melanocytes contribute to elastogenesis in the developing murine aortic valve. *Scientific Reports*, *14*(1), 25481. https://doi.org/10.1038/s41598-024-73673-5

O’Brien, K. D., Probstfield, J. L., Caulfield, M. T., Nasir, K., Takasu, J., Shavelle, D. M., Wu, A. H., Zhao, X.-Q., & Budoff, M. J. (2005). Angiotensin-converting enzyme inhibitors and change in aortic valve calcium. *Archives of Internal Medicine*, *165*(8), 858–862. https://doi.org/10.1001/archinte.165.8.858

Osnabrugge, R. L. J., Mylotte, D., Head, S. J., Van Mieghem, N. M., Nkomo, V. T., LeReun, C. M., Bogers, A. J. J. C., Piazza, N., & Kappetein, A. P. (2013). Aortic Stenosis in the Elderly: Disease Prevalence and Number of Candidates for Transcatheter Aortic Valve Replacement: A Meta-Analysis and Modeling Study. *Journal of the American College of Cardiology*, *62*(11), 1002–1012. https://doi.org/10.1016/j.jacc.2013.05.015

Otto, C. M., Nishimura, R. A., Bonow, R. O., Carabello, B. A., Erwin, J. P., Gentile, F., Jneid, H., Krieger, E. V., Mack, M., McLeod, C., O’Gara, P. T., Rigolin, V. H., Sundt, T. M., Thompson, A., & Toly, C. (2021). 2020 ACC/AHA Guideline for the Management of Patients With Valvular Heart Disease: A Report of the American College of Cardiology/American Heart Association Joint Committee on Clinical Practice Guidelines. *Journal of the American College of Cardiology*, *77*(4), e25–e197. https://doi.org/10.1016/j.jacc.2020.11.018

Paulos, C. M., Turk, M. J., Breur, G. J., & Low, P. S. (2004). Folate receptor-mediated targeting of therapeutic and imaging agents to activated macrophages in rheumatoid arthritis. *Advanced Drug Delivery Reviews*, *56*(8), 1205–1217. https://doi.org/10.1016/j.addr.2004.01.012

Pawade, T. A., Cartlidge, T. R. G., Jenkins, W. S. A., Adamson, P. D., Robson, P., Lucatelli, C., Van Beek, E. J. R., Prendergast, B., Denison, A. R., Forsyth, L., Rudd, J. H. F., Fayad, Z. A., Fletcher, A., Tuck, S., Newby, D. E., & Dweck, M. R. (2016). Optimization and Reproducibility of Aortic Valve 18F-Fluoride Positron Emission Tomography in Patients With Aortic Stenosis. *Circulation: Cardiovascular Imaging*, *9*(10), e005131. https://doi.org/10.1161/CIRCIMAGING.116.005131

Pawade, T. A., Newby, D. E., & Dweck, M. R. (2015). Calcification in Aortic Stenosis: The Skeleton Key. *Journal of the American College of Cardiology*, *66*(5), 561–577. https://doi.org/10.1016/j.jacc.2015.05.066

Peet, C., Ivetic, A., Bromage, D. I., & Shah, A. M. (2020). Cardiac monocytes and macrophages after myocardial infarction. *Cardiovascular Research*, *116*(6), 1101. https://doi.org/10.1093/cvr/cvz336

Peltonen, T., Näpänkangas, J., Ohtonen, P., Aro, J., Peltonen, J., Soini, Y., Juvonen, T., Satta, J., Ruskoaho, H., & Taskinen, P. (2011). (Pro)renin receptors and angiotensin converting enzyme 2/angiotensin-(1-7)/Mas receptor axis in human aortic valve stenosis. *Atherosclerosis*, *216*(1), 35–43. https://doi.org/10.1016/j.atherosclerosis.2011.01.018

Qureshi, A. T., Chen, C., Shah, F., Thomas-Porch, C., Gimble, J. M., & Hayes, D. J. (2014). Chapter Five—Human Adipose-Derived Stromal/Stem Cell Isolation, Culture, and Osteogenic Differentiation. In O. A. MacDougald (Ed.), *Methods in Enzymology* (Vol. 538, pp. 67–88). Academic Press. https://doi.org/10.1016/B978-0-12-800280-3.00005-0

Rader, F., Sachdev, E., Arsanjani, R., & Siegel, R. J. (2015). Left Ventricular Hypertrophy in Valvular Aortic Stenosis: Mechanisms and Clinical Implications. *The American Journal of Medicine*, *128*(4), 344–352. https://doi.org/10.1016/j.amjmed.2014.10.054

Rajamannan, N. M., Evans, F. J., Aikawa, E., Grande-Allen, K. J., Demer, L. L., Heistad, D. D., Simmons, C. A., Masters, K. S., Mathieu, P., O’Brien, K. D., Schoen, F. J., Towler, D. A., Yoganathan, A. P., & Otto, C. M. (2011). Calcific Aortic Valve Disease: Not Simply a Degenerative Process A Review and Agenda for Research from the National Heart and Lung and Blood Institute Aortic Stenosis Working Group. *Circulation*, *124*(16), 1783–1791. https://doi.org/10.1161/CIRCULATIONAHA.110.006767

Rajamannan, N. M., Subramaniam, M., Rickard, D., Stock, S. R., Donovan, J., Springett, M., Orszulak, T., Fullerton, D. A., Tajik, A. J., Bonow, R. O., & Spelsberg, T. (2003). Human aortic valve calcification is associated with an osteoblast phenotype. *Circulation*, *107*(17), 2181–2184. Scopus. https://doi.org/10.1161/01.CIR.0000070591.21548.69

Rossebø, A. B., Pedersen, T. R., Boman, K., Brudi, P., Chambers, J. B., Egstrup, K., Gerdts, E., Gohlke-Bärwolf, C., Holme, I., Kesäniemi, Y. A., Malbecq, W., Nienaber, C. A., Ray, S., Skjærpe, T., Wachtell, K., & Willenheimer, R. (2008). Intensive lipid lowering with simvastatin and ezetimibe in aortic stenosis. *New England Journal of Medicine*, *359*(13), 1343–1356. Scopus. https://doi.org/10.1056/NEJMoa0804602

Roth, G. A., Mensah, G. A., Johnson, C. O., Addolorato, G., Ammirati, E., Baddour, L. M., Barengo, N. C., Beaton, A. Z., Benjamin, E. J., Benziger, C. P., Bonny, A., Brauer, M., Brodmann, M., Cahill, T. J., Carapetis, J., Catapano, A. L., Chugh, S. S., Cooper, L. T., Coresh, J., … Fuster, V. (2020). Global Burden of Cardiovascular Diseases and Risk Factors, 1990–2019: Update From the GBD 2019 Study. *Journal of the American College of Cardiology*, *76*(25), 2982–3021. https://doi.org/10.1016/j.jacc.2020.11.010

Saeed, Y., Lythgoe, D., Garg, P., & Chuah, S. (2012). 077 Osteoporosis and bisphosphonate's use associated with reduced progression of calcific aortic stenosis: Retrospective observational single centre study. *Heart*, *98*(Suppl 1), A44–A44. https://doi.org/10.1136/heartjnl-2012-301877b.77

Scatena, M., Jackson, M. F., Speer, M. Y., Leaf, E. M., Wallingford, M. C., & Giachelli, C. M. (2018). Increased Calcific Aortic Valve Disease in response to a diabetogenic, procalcific diet in the LDLr -/- ApoB 100/100 mouse model. *Cardiovascular Pathology*, *34*, 28–37. https://doi.org/10.1016/j.carpath.2018.02.002

Shigeta, A., Huang, V., Zuo, J., Basada, R., Nakashima, Y., Lu, Y., Ding, Y., Pellegrini, M., Kulkarni, R. P., Hsiai, T., Deb, A., Zhou, B., Nakano, H., & Nakano, A. (2019). Endocardially-derived macrophages are essential for valvular remodeling. *Developmental Cell*, *48*(5), 617-630.e3. https://doi.org/10.1016/j.devcel.2019.01.021

Silvola, J. M. U., Li, X.-G., Virta, J., Marjamäki, P., Liljenbäck, H., Hytönen, J. P., Tarkia, M., Saunavaara, V., Hurme, S., Palani, S., Hakovirta, H., Ylä-Herttuala, S., Saukko, P., Chen, Q., Low, P. S., Knuuti, J., Saraste, A., & Roivainen, A. (2018). Aluminum fluoride-18 labeled folate enables in vivo detection of atherosclerotic plaque inflammation by positron emission tomography. *Scientific Reports*, *8*(1), 9720. https://doi.org/10.1038/s41598-018-27618-4

Skytthe, M. K., Graversen, J. H., & Moestrup, S. K. (2020). Targeting of CD163+ Macrophages in Inflammatory and Malignant Diseases. *International Journal of Molecular Sciences*, *21*(15), 5497. https://doi.org/10.3390/ijms21155497

Stein, E. J., Fearon, W. F., Elmariah, S., Kim, J. B., Kapadia, S., Kumbhani, D. J., Gillam, L., Whisenant, B., Quader, N., Zajarias, A., Welt, F. G., Bavry, A. A., Coylewright, M., Piana, R. N., Mallugari, R. R., Clark, D. E., Patel, J. N., Gonzales, H., Gupta, D. K., … Lindman, B. R. (2022). Left Ventricular Hypertrophy and Biomarkers of Cardiac Damage and Stress in Aortic Stenosis. *Journal of the American Heart Association*, *11*(7), e023466. https://doi.org/10.1161/JAHA.121.023466

Syväranta, S., Helske, S., Laine, M., Lappalainen, J., Kupari, M., Mäyränpää, M. I., Lindstedt, K. A., & Kovanen, P. T. (2010). Vascular endothelial growth factor-secreting mast cells and myofibroblasts: A novel self-perpetuating angiogenic pathway in aortic valve stenosis. *Arteriosclerosis, Thrombosis, and Vascular Biology*, *30*(6), 1220–1227. https://doi.org/10.1161/ATVBAHA.109.198267

Tastet, L., Capoulade, R., Clavel, M.-A., Larose, É., Shen, M., Dahou, A., Arsenault, M., Mathieu, P., Bédard, É., Dumesnil, J. G., Tremblay, A., Bossé, Y., Després, J.-P., & Pibarot, P. (2017).

Systolic hypertension and progression of aortic valve calcification in patients with aortic stenosis: Results from the PROGRESSA study. *European Heart Journal - Cardiovascular Imaging*, *18*(1), 70–78. https://doi.org/10.1093/ehjci/jew013

Townsend, D. W., Besozzi, M. C., & Carney, J. P. J. (2007). Integrated PET/CT. In M. F. Di Carli & M. J. Lipton (Eds.), *Cardiac PET and PET/CT Imaging* (pp. 34–45). Springer. https://doi.org/10.1007/978-0-387-38295-1_3

Tzolos, E., & Dweck, M. R. (2020). 18F-Sodium Fluoride (18F-NaF) for Imaging Microcalcification Activity in the Cardiovascular System. *Arteriosclerosis, Thrombosis, and Vascular Biology*, *40*(7), 1620–1626. https://doi.org/10.1161/ATVBAHA.120.313785

Vahanian, A., Beyersdorf, F., Praz, F., Milojevic, M., Baldus, S., Bauersachs, J., Capodanno, D., Conradi, L., De Bonis, M., De Paulis, R., Delgado, V., Freemantle, N., Gilard, M., Haugaa, K. H., Jeppsson, A., Jüni, P., Pierard, L., Prendergast, B. D., Sádaba, J. R., … ESC National Cardiac Societies. (2022). 2021 ESC/EACTS Guidelines for the management of valvular heart disease: Developed by the Task Force for the management of valvular heart disease of the European Society of Cardiology (ESC) and the European Association for Cardio-Thoracic Surgery (EACTS). *European Heart Journal*, *43*(7), 561–632. https://doi.org/10.1093/eurheartj/ehab395

Vemulapalli Sreekanth, Carroll John D., Mack Michael J., Li Zhuokai, Dai David, Kosinski Andrzej S., Kumbhani Dharam J., Ruiz Carlos E., Thourani Vinod H., Hanzel George, Gleason Thomas G., Herrmann Howard C., Brindis Ralph G., & Bavaria Joseph E. (2019). Procedural Volume and Outcomes for Transcatheter Aortic-Valve Replacement. *New England Journal of Medicine*, *380*(26), 2541–2550. https://doi.org/10.1056/NEJMsa1901109

Villa-Bellosta, R. (2021). Vascular Calcification: Key Roles of Phosphate and Pyrophosphate. *International Journal of Molecular Sciences*, *22*(24), 13536. https://doi.org/10.3390/ijms222413536

Wong, M., Staszewsky, L., Latini, R., Barlera, S., Volpi, A., Chiang, Y.-T., Benza, R. L., Gottlieb, S. O., Kleemann, T. D., Rosconi, F., Vandervoort, P. M., Cohn, J. N., & Val-HeFT Heart Failure Trial Investigators. (2002). Valsartan benefits left ventricular structure and function in heart failure: Val-HeFT echocardiographic study. *Journal of the American College of Cardiology*, *40*(5), 970–975. https://doi.org/10.1016/s0735-1097(02)02063-6

Zacchigna, S., Paldino, A., Falcão-Pires, I., Daskalopoulos, E. P., Dal Ferro, M., Vodret, S., Lesizza, P., Cannatà, A., Miranda-Silva, D., Lourenço, A. P., Pinamonti, B., Sinagra, G., Weinberger, F., Eschenhagen, T., Carrier, L., Kehat, I., Tocchetti, C. G., Russo, M., Ghigo, A., … Thum, T. (2021). Towards standardization of echocardiography for the evaluation of left ventricular function in adult rodents: A position paper of the ESC Working Group on Myocardial Function. *Cardiovascular Research*, *117*(1), 43–59. https://doi.org/10.1093/cvr/cvaa110

Zheng, K. H., Tsimikas, S., Pawade, T., Kroon, J., Jenkins, W. S. A., Doris, M. K., White, A. C., Timmers, N. K. L. M., Hjortnaes, J., Rogers, M. A., Aikawa, E., Arsenault, B. J., Witztum, J. L., Newby, D. E., Koschinsky, M. L., Fayad, Z. A., Stroes, E. S. G., Boekholdt, S. M., & Dweck, M. R. (2019). Lipoprotein(a) and Oxidized Phospholipids Promote Valve Calcification in Patients With Aortic Stenosis. *Journal of the American College of Cardiology*, *73*(17), 2150–2162. https://doi.org/10.1016/j.jacc.2019.01.070

Zheng, K. H., Tzolos, E., & Dweck, M. R. (2020). Pathophysiology of Aortic Stenosis and Future Perspectives for Medical Therapy. *Cardiology Clinics*, *38*(1), 1–12. https://doi.org/10.1016/j.ccl.2019.09.010